

A Universal Protocol for Quantum-Enhanced Sensing via Information Scrambling

Bryce Kobrin,^{1,*} Thomas Schuster,^{2,1,*} Maxwell Block,³ Weijie Wu,³ Bradley Mitchell,⁴ Emily Davis,^{3,5} and Norman Y. Yao³

¹*Department of Physics, University of California Berkeley, Berkeley, CA 94720, USA*

²*Walter Burke Institute for Theoretical Physics and Institute for Quantum Information and Matter, California Institute of Technology, Pasadena, CA 91125 USA*

³*Department of Physics, Harvard University, Cambridge, MA 02138, USA*

⁴*IBM Quantum, IBM Almaden Research Center, San Jose, CA 95120, USA*

⁵*Department of Physics, New York University, New York, NY, 10003, USA*

We introduce a novel protocol, which enables Heisenberg-limited quantum-enhanced sensing using the dynamics of any interacting many-body Hamiltonian. Our approach—dubbed *butterfly metrology*—utilizes a single application of forward and reverse time evolution to produce a coherent superposition of a “scrambled” and “unscrambled” quantum state. In this way, we create metrologically-useful long-range entanglement from generic local quantum interactions. The sensitivity of butterfly metrology is given by a sum of local out-of-time-order correlators (OTOCs)—the prototypical diagnostic of quantum information scrambling. Our approach broadens the landscape of platforms capable of performing quantum-enhanced metrology; as an example, we provide detailed blueprints and numerical studies demonstrating a route to scalable quantum-enhanced sensing in ensembles of solid-state spin defects.

Quantum-enhanced metrology leverages entanglement in a many-body system to improve the fundamental precision of sensing [1–4]. The realization of this enhancement with large numbers of interacting particles represents an ongoing objective, with a wide range of potential applications including atomic time-keeping [5–7], gravitational wave sensing [8–10], biological imaging [11–14], and the search for new fundamental physics [15–18].

From a theoretical perspective, the requirements for a many-body state to exhibit “metrologically-useful” entanglement are well understood [4, 19–23]. However, from an experimental perspective, two overarching challenges limit the range of experimental platforms that can realize this advantage: state preparation and signal readout. For the latter, the key tension is that any *direct* measurement on a metrologically useful state will also be highly susceptible to noise in the read-out process [24, 25]. To address this challenge, seminal recent results have introduced sensing protocols that rely on *time-reversed* dynamics [21, 26–28]. Crucially, these protocols exhibit significantly improved robustness to readout noise and have been experimentally realized in the context of both spin squeezed [29] and GHZ states [30].

For the former challenge, one of the most natural strategies to prepare a metrologically useful state is simply to perform Hamiltonian time evolution from an initial product state; however, the class of Hamiltonians for which this succeeds is extremely limited [4]. Indeed, the only known examples consist of large- S spin models [31–36], symmetry breaking evolution from a pure state [37], and commuting central spin models [26]. This precisely encodes the challenge that while most quantum states are highly entangled, only a vanishingly small subset can be utilized to perform enhanced sensing [38].

In this Letter, we introduce a novel sensing protocol,

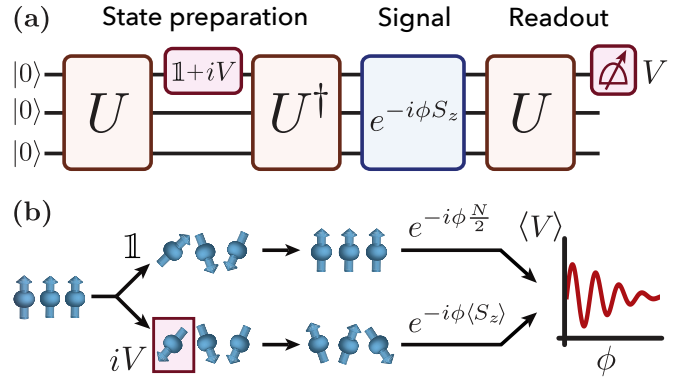


FIG. 1. (a) Schematic quantum circuit depicting our butterfly metrology protocol with local controls. The “butterfly state” is prepared via forward and reverse time evolution under a many-body Hamiltonian, $U = e^{-iHt}$, interleaved with a local rotation, $(\mathbb{1} + iV)/\sqrt{2}$. The external signal, $e^{-i\phi S_z}$, is detected by evolving forward once more and measuring the local observable V . (b) In effect, the protocol performs interferometry between two quantum trajectories. In the first (top), the forward and reverse evolution cancel, yielding the polarized state $|0\rangle$. In the second (bottom), the perturbation iV disrupts this cancellation, yielding the “scrambled” state, $iV(t)|0\rangle$. The two states acquire macroscopically different phases under the signal whenever U is scrambling.

dubbed “butterfly metrology”. Crucially, our protocol enables the preparation of metrologically-useful entangled states (from an initial product state) using completely *generic* many-body Hamiltonians; in fact, our approach works for essentially any Hamiltonian, so long as it is not localized [39]. The key insight underlying our approach is to use time reversal not only to detect, but also to *prepare* the metrological state (Fig. 1). By doing so, our protocol generates a GHZ-like state from the dynam-

ics of almost any Hamiltonian. This state is a coherent superposition of a fully polarized state and a *scrambled* state [Fig. 1(b)]. The latter has zero polarization on average, enabling our protocol to achieve sensitivities within a factor of two of the fundamental Heisenberg limit.

Our main results are threefold. First, we establish a precise connection between butterfly metrology and quantum information scrambling [40]. In particular, we demonstrate that our protocol’s sensitivity is exactly given by a sum of local out-of-time-order correlation functions (OTOCs)—the standard probe of scrambling dynamics [41–43]. For fully scrambling dynamics, we immediately obtain a measurement sensitivity, η , that exhibits a Heisenberg scaling (i.e. $\eta \approx 2/N$), with the number of particles. Second, we introduce a variant of our protocol that utilizes only *global* control and readout, significantly reducing the experimental requirements. Finally, we highlight the broad applicability of our approach by providing detailed blueprints and numerical simulations for a variety of experimental platforms [44]. A particularly clear advantage over existing protocols is shown in the case of solid-state spin defects [45–47].

General strategy—Consider an ensemble of N spin-1/2 particles attempting to sense a weak external signal. We imagine that the sensors are coupled to the signal, ϕ , via the collective spin operator $S_z = \frac{1}{2} \sum_i \sigma_i^z$, where σ_i^z is a local Pauli operator acting on spin i . A generic sensing protocol has three steps: (i) prepare a state, $|\psi\rangle$, on the N spins, (ii) accumulate the signal, $e^{-i\phi S_z}$, and (iii) read-out an observable M on the resulting state. The goal of any quantum sensing protocol is to optimize the sensitivity, $\eta = \Delta M_\phi / \partial_\phi \langle M \rangle_\phi$, of the measured expectation value, $\langle M \rangle_\phi$, to the signal ϕ , where ΔM is the standard deviation of M .

The optimal sensitivity, over all possible observables, is lower-bounded by a property of the state $|\psi\rangle$, namely, the so-called quantum Fisher information (QFI) [48]. For pure states, the QFI, \mathcal{F} , is simply given by twice the variance of the operator that couples to the signal, in our case, S_z . This immediately yields a lower bound: $\eta \geq 1/\sqrt{\mathcal{F}} \equiv 1/(2\Delta S_z)$.

To provide a bit of intuition, let us consider how η behaves in a few specific cases. For a product state, the standard deviation, ΔS_z , is at most \sqrt{N} , implying a sensitivity scaling as, $\eta \sim 1/\sqrt{N}$, commonly known as the standard quantum limit (SQL). Most quantum states, despite being highly entangled, do not surpass this scaling. Indeed, a Haar-random state possesses, on average, the same QFI as an unentangled state [44]. On the other hand, the paradigmatic GHZ state, $(|0\rangle^{\otimes N} + |1\rangle^{\otimes N})/\sqrt{2}$, exhibits maximal correlations in the z -basis, and thus a standard deviation $\Delta S_z = N/2$ [49]; this yields a sensitivity, $\eta = 1/N$, known as the Heisenberg limit [50].

Our approach begins by introducing a new class of

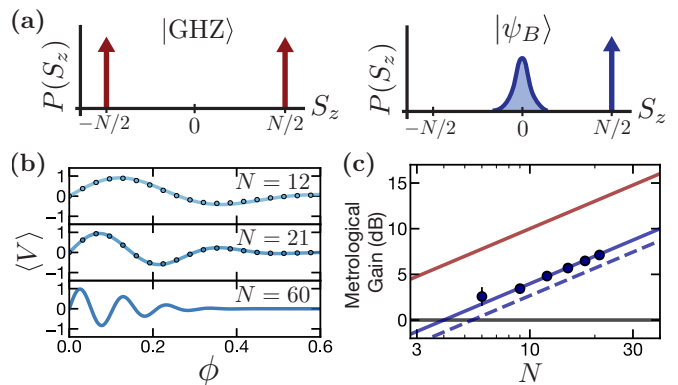


FIG. 2. (a) Schematic of the polarization distribution, $P(S_z)$, of the GHZ state (left) and the butterfly state (right). The former features two maximally separated peaks at $S_z = \pm N/2$; this leads to an optimal sensitivity, $\eta^{-1} = N$. The latter features a narrow peak at $N/2$ and a broader peak at zero; this leads to a sensitivity, $\eta^{-1} \approx N/2$. (b) Numerical plot of the local expectation value, $\langle V \rangle_\phi$, as a function of the signal strength, ϕ , when U is Haar-random (solid lines) and when U corresponds to evolution under a generic spin chain Hamiltonian for long times (dots) [44]. The expectation value undergoes damped oscillations with frequency $\approx N/2$. (c) The metrological gain, $1/(N\eta^2)$, of butterfly metrology with local controls for a generic spin chain Hamiltonian as a function of system size (dots). The Heisenberg limit (red), standard quantum limit (black), and Haar-random predictions for local (solid blue) and global (dashed blue) butterfly metrology are shown for comparison.

metrological state, which we call the ‘butterfly state’:

$$|\psi_B\rangle = \frac{|\mathbf{0}\rangle + iV(t)|\mathbf{0}\rangle}{\sqrt{2}}. \quad (1)$$

Here, $|\mathbf{0}\rangle \equiv |0\rangle^{\otimes N}$ is the fully polarized state, and $V(t) = U^\dagger V U$ is a local Pauli operator (e.g. $V = \sigma_0^x$) evolved under a unitary, U . We envision $U = e^{-iHt}$ to be generated by time evolution via a generic, many-body Hamiltonian, H . For sufficiently late times, U is “fully scrambling” and resembles a Haar-random unitary. As depicted in Fig. 1(a), $|\psi_B\rangle$ can be prepared by applying a local rotation $(\mathbb{1} + iV)/\sqrt{2}$ (i.e. a $\pi/2$ -pulse), sandwiched between forward and backward time evolution.

Physically, the butterfly state is a superposition between two quantum trajectories generated by the two terms, $\mathbb{1}$ and iV , of the local rotation [Fig. 1(a)]. In the first, the forward and backward evolution perfectly cancel, returning the system to the polarized state. In the second, the local operator iV disrupts this cancellation. When U is fully scrambling, this disruption will propagate to every spin in the system, and the second trajectory will resemble a Haar-random state, with an average polarization of zero. Thus, much like the GHZ state, the butterfly state $|\psi_B\rangle$ is a superposition of two states with a macroscopic difference, $\approx N/2$, in polarization [Fig. 2(a)]. This yields a standard deviation, $\Delta S_z \approx N/4$, and thus

an optimal sensitivity of $\eta \approx 2/N$, a mere factor of two from the Heisenberg limit.

Measurement protocol—Having defined the butterfly state and its optimal sensitivity, we now devise an explicit protocol for measuring the external signal, ϕ . The simplest conceptual approach is to directly extract ϕ from a measurement on the perturbed state. However, this will require probing highly non-local coherences between the two trajectories in $|\psi\rangle_B$. This is even more difficult in our setting, compared to that of the GHZ state, since the second trajectory in $|\psi\rangle_B$ is a highly-entangled scrambled state.

To this end, we propose an alternative approach where we perform a final step of time evolution under U after the signal has been acquired [Fig. 1(a)], and then conclude by measuring the *local* operator $M \equiv V$ [51]. This produces an expectation value,

$$\langle V \rangle_\phi = \frac{1}{2} \langle \mathbf{0} | V(t) | \mathbf{0} \rangle - \frac{1}{2} \langle \mathbf{0} | V(t) e^{i\phi S_z} V(t) e^{-i\phi S_z} V(t) | \mathbf{0} \rangle + \text{Im} \left[e^{i\phi N/2} \langle \mathbf{0} | V(t) e^{-i\phi S_z} V(t) | \mathbf{0} \rangle \right]. \quad (2)$$

For a small signal ϕ , the first and second terms cancel, giving $\langle V \rangle_\phi \approx \phi(N/2 - \langle \mathbf{0} | V(t) S_z V(t) | \mathbf{0} \rangle)$, and thus a sensitivity,

$$\eta_{\phi=0}^{-1} = N/2 - \langle \mathbf{0} | V(t) S_z V(t) | \mathbf{0} \rangle, \quad (3)$$

which is precisely equal to the difference in polarization between the two trajectories in $|\psi_B\rangle$. When the unitary is fully scrambling, the state $V(t) | \mathbf{0} \rangle$, has a mean polarization of zero, and our measurement protocol gives $\eta_{\phi=0} \approx 2/N$; this saturates the optimal sensitivity allowed by the butterfly state's QFI.

Sensitivity from operator growth—Thus far, we have focused on late times where the unitary U is *fully* scrambling. To characterize the sensitivity at earlier times, we leverage a precise connection between the sensitivity and information scrambling. In particular, using $\sigma_i^z | \mathbf{0} \rangle = 1$, one can re-write

$$\eta_{\phi=0}^{-1} = \frac{1}{2} \sum_i (1 - \langle \mathbf{0} | \sigma_i^z V(t) \sigma_i^z V(t) | \mathbf{0} \rangle), \quad (4)$$

where the expectation values correspond to local out-of-time-order correlation functions (OTOCs) [41–43].

These OTOCs quantify whether the time-evolved perturbation, $V(t)$, commutes with each spin operator σ_i^z . As a function of time, each OTOC begins at unity and decays to zero as $V(t)$ grows to have support on spin i [52–54]. Thus, the sum in Eq. (4) counts the number of spins, \mathcal{S} , within the support of $V(t)$. Intuitively, the operator $V(t)$ scrambles each spin within its support, effectively randomizing its polarization. This leads to a polarization difference $\sim \mathcal{S}/2$ between the scrambled state, $V(t) | \mathbf{0} \rangle$, and the fully polarized state, $| \mathbf{0} \rangle$, yielding a sensitivity $\eta \approx 2/\mathcal{S}$.

To this end, in order to evaluate the sensitivity of butterfly metrology at earlier times, one simply needs to understand the dynamics of operator growth under the Hamiltonian, H . For Hamiltonians with local interactions, the operator support typically grows ballistically in time, $\mathcal{S} \approx (v_B t)^d$, where d is the spatial dimension and v_B is known as the butterfly velocity. This growth continues until the so-called *scrambling time*, $t_s \approx v_B^{-1} N^{1/d}$, after which the unitary is fully scrambling and the operator has support on the entire system, $\mathcal{S} \approx N$. This leads to a sensitivity:

$$\eta \approx \begin{cases} 2/(v_B t)^d, & t \lesssim t_s \\ 2/N, & t \gtrsim t_s, \end{cases} \quad (5)$$

which continuously improves as a function of time and saturates to its optimal value at t_s [Fig. 2(d)].

A few remarks are in order. First, for Hamiltonians with long-range interactions, operators may exhibit faster-than-ballistic growth [55]. For instance, under all-to-all-interactions, operators typically grow exponentially in time, $\mathcal{S} \sim e^{\lambda t}$, where λ is the Lyapunov exponent [56, 57]. This leads to a more rapid improvement in the sensitivity and an earlier saturation to its optimal value.

Second, let us analyze the *dynamic range* of butterfly metrology, i.e. its behavior at larger values of ϕ . As per Eq. (2), this naturally requires us to consider the polarization distribution, $P(S_z)$, of the scrambled trajectory [Fig. 2(a)]. For a Haar-random state, this polarization distribution is a Gaussian with mean zero and width $\sim \sqrt{N}$. When the signal is small compared to this width, $\phi \ll 1/\sqrt{N}$, one can approximate $e^{i\phi S_z} V(t) | \mathbf{0} \rangle \approx V(t) | \mathbf{0} \rangle$, leading to a sinusoidal expectation value $\langle V \rangle_\phi \approx \sin(\phi N/2)$ [Fig. 2(b)], and a Heisenberg-scaling sensitivity. For larger signal strengths, $\phi \gtrsim 1/\sqrt{N}$, this approximation breaks down and we find that the magnitude of the oscillations, and thus, the sensitivity, gradually decays to zero [Fig. 2(b)].

Finally, the presence of conservation laws in the Hamiltonian will cause the sensitivity to deviate slightly from our estimates above. In particular, since time evolution cannot change the expectation value of any conserved quantity, the scrambled butterfly trajectory will generally not approach a Haar-random state. Instead, it will resemble a random state drawn from the Gibbs ensemble determined by the values of each conserved quantity in the initial state $| \mathbf{0} \rangle$. At late times, this still leads to a Heisenberg-scaling sensitivity, but with a pre-factor determined by the polarization density, m , of the Gibbs state, $\eta^{-1} \approx N(1-m)/2$.

Butterfly metrology with global controls—Our discussions above have focused on the use of local controls within the butterfly metrology protocol: a local rotation to prepare the state, $|\psi_B\rangle$, and a local measurement to extract the signal, ϕ . We now demonstrate a variant of

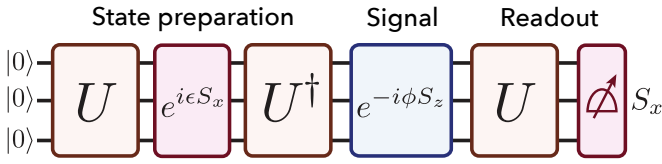


FIG. 3. Schematic of butterfly metrology with global controls. The metrological state is prepared using a global rotation, $e^{i\epsilon S_x}$, under the spin operator $S_x = \frac{1}{2} \sum_i \sigma_i^x$, and the signal is readout via the global expectation value, $\langle S_x \rangle$.

our protocol that utilizes purely global controls (Fig. 3); this is particularly important from an experimental perspective and allows butterfly metrology to be deployed in platforms without single-site addressing [27, 58].

In particular, instead of applying a local $\pi/2$ -pulse to prepare the butterfly state (Fig. 1), one applies the global rotation $e^{i\epsilon S_x}$, with $S_x = \frac{1}{2} \sum_i \sigma_i^x$. Similarly, in order to readout this signal, one measures the total polarization along the x -direction, $\langle S_x \rangle$.

To build some intuition for the sensitivity of our global butterfly metrology protocol, let us consider two limits. First, consider the “trivial” limit where $t = 0$ and $U = \mathbb{1}$. By setting $\epsilon = \pi/4$, one immediately recognizes that our protocol reduces to N parallel copies of Ramsey spectroscopy, and thus exhibits an SQL-scaling sensitivity, $\eta \sim 1/\sqrt{N}$.

Second, consider the late-time limit where U is fully scrambling. Much as before, we decompose the global rotation into an identity and non-identity component, $e^{i\epsilon S_x} \equiv a\mathbb{1} + i\tilde{V}$, where $a = \cos^N(\epsilon)$ and \tilde{V} is traceless. This leads to the “global” butterfly state,

$$|\tilde{\psi}_B\rangle = a|\mathbf{0}\rangle + i\tilde{V}(t)|\mathbf{0}\rangle. \quad (6)$$

In order to maximize the sensitivity of our global protocol, we set $\epsilon \sim 1/\sqrt{N}$ so that the butterfly state, $|\tilde{\psi}_B\rangle$, is an approximately equal superposition of its two trajectories. More specifically, we find that the optimal value occurs at $\epsilon = 1/\sqrt{2N}$, which yields a Heisenberg-scaling sensitivity, $\eta = \sqrt{2e}/N \approx 2.3/N$ [44]. We note that this is nearly identical to the late-time sensitivity obtained in our local protocol [Eq. (5)].

As one evolves from time $t = 0$ to the scrambling time $t = t_s$, the sensitivity smoothly interpolates between the two limits above. This interpolation can again be understood in the language of operator growth; indeed, at intermediate times, the sensitivity is given by $\eta \sim 1/\sqrt{N\mathcal{S}}$, where \mathcal{S} is the number of spins in the support of a time-evolved local operator [44].

Experimental proposals—Perhaps the most unique feature of butterfly metrology is its universality—the protocol utilizes evolution under a generic many-body Hamiltonian and thus, can naturally be realized in a wide variety of experimental platforms (Table I). Here, we focus on the setting of solid-state spin ensembles [59],

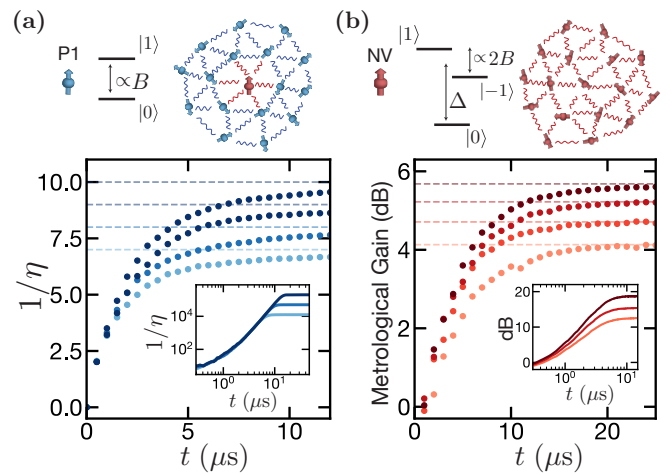


FIG. 4. Numerical simulations for the sensing protocol under the dynamics of two experimental platforms. (a) The sensitivity of our protocol with *local* controls for a hybrid spin system, consisting of a single NV center surrounded by a cluster of P1 centers. The simulations are performed via exact diagonalization with $N \in [14, 20]$ total spins. After an initial growth period, the sensitivity saturates at $\eta = 2/N$ (dashed line), consistent with our expectation for fully scrambled dynamics. The inset displays the sensitivity for large-scale systems, $N \sim 10^4 - 10^5$, simulated via a stochastic growth model [44]. (b) The metrological gain, $1/(N\eta^2)$, and sensitivity (inset) of our protocol with *global* controls implemented for a dense ensemble of NV centers. The total number of spins is $N \in [14, 20]$ spins. For both systems, the density of spin defects is 100 ppm, corresponding to an average separation of ~ 4 nm.

where achieving quantum-enhanced sensitivities remains an outstanding challenge [26, 60, 61]. A key part of this challenge stems from the nature of the dipolar interaction intrinsic to such systems. Indeed, for disordered spin ensembles, the dipolar Hamiltonian, while strongly-interacting, is far from the conventional all-to-all-coupled models (e.g. one-axis twisting) typically used to generate metrologically-useful entanglement [27, 29].

To this end, we propose and analyze two implementations of butterfly metrology using dense ensembles of nitrogen-vacancy (NV) color centers in diamond [59, 62]. NV centers behave as sensitive magnetometers and have been used to detect a variety of external signals, ranging from neuronal action potentials to superconducting vortices [63, 64]. Each NV exhibits a spin, $S = 1$, electronic ground state [Fig. 4(b)], which can be optically polarized and read out at room temperature. In the absence of an external magnetic field, the NV’s spin sublevels are separated by $\Delta = 2.87$ GHz, corresponding to the zero-field splitting [59].

In addition to NV centers, the diamond sample also contains a relatively high concentration of optically-dark, spin-1/2 P1 centers (substitutional nitrogen impurities). Indeed, each NV center is typically surrounded by a large

| Experimental platform | Control | Time-reversal method |
|------------------------------|---------|----------------------|
| Hybrid NV-P1 system [66] | Local | Hamiltonian eng. |
| NV-center ensemble [69] | Global | Hamiltonian eng. |
| Dipolar Rydberg atoms [71] | Both | State encoding |
| Atoms in optical cavity [72] | Global | Laser detuning |
| Superconducting qubits [73] | Both | π -pulse |
| Trapped ions [74, 75] | Both | Laser phase |

TABLE I. Butterfly metrology with either local or global controls can be realized in a wide array of experimental platforms. Detailed blueprints and discussions are provided in the supplemental materials [44].

bath of P1 spins [Fig. 4(a)] [65, 66]. Conventionally, such P1s are viewed as a source of decoherence and dynamical decoupling is employed to suppress their interactions with NVs [67].

For our first implementation, we describe a realization of butterfly metrology (with local controls) in a hybrid NV-P1 system, where the NV center provides the local control and the P1 centers comprise the remaining spins [Fig. 4(a)]. We envision an experimental scenario where the P1 centers are polarized either by working at cryogenic temperatures or via Hartmann-Hahn hyperpolarization [68]. For external magnetic fields, B , away from level anti-crossing, the NV center is off-resonant from the P1s, enabling the application of selective local rotations via microwave fields. This off-resonance also affects the many-body interactions in the system: the P1s interact with one another via the full magnetic dipolar interaction, and with the NV, via the Ising term of this interaction [44]. Crucially, both of these interactions can be time reversed using a simple generalization of the so-called WAHUA pulse sequence [44].

For our second implementation, we consider a scenario where the NV-P1 interactions have been dynamically decoupled, leaving only interactions *between* NV centers themselves [69, 70]. This scenario is naturally suited to the global-variant of butterfly metrology [Fig. 3]. In particular, we envision applying a global rotation on the entire ensemble of NV centers using a microwave pulse. As before, time-reversed dynamics can be achieved via Hamiltonian engineering techniques [44].

To explore the dynamics of the sensitivity in both implementations, we perform an extensive set of numerical simulations using both Krylov subspace methods (for smaller system sizes) and a stochastic model for operator growth (for larger system sizes) [55, 76, 77]. For our hybrid NV-P1 approach [Fig. 4(a)], the sensitivity improves rapidly in time and saturates at $\eta \approx 2/N$, consistent with our previous analysis. The sensitivity dynamics of our global NV-based approach [Fig. 4(b)] are somewhat similar. In this case, we plot the metrological gain, $G = \eta^{-2}/N$, which saturates at $G \approx (0.43)^2 N$ and quantifies the enhancement compared to the stan-

dard quantum limit [78]. Interestingly, for larger system sizes (up to $\sim 10^6$ spins), we find that both the sensitivity (local variant) and metrological gain (global variant) exhibit a sustained period of super-polynomial growth. This arises from the Levy flight growth of operators in 3D with $1/r^3$ interactions [55].

Much like other time-reversal-based sensing protocols [26, 27], butterfly metrology maintain a Heisenberg-limited sensitivity in the presence of both read-out and initialization errors. Our protocol is particularly robust against coherent errors that can be time reversed; for example, slow variations in the Hamiltonian parameters [74]. The effect of incoherent errors can be understood using our framework of operator growth, namely, they suppress the sensitivity by a factor $\sim e^{-4\gamma \int_0^t dt' \mathcal{S}(t')}$ [79], where γ is the local noise rate and $\mathcal{S}(t)$ is the operator support [44, 80].

Our work opens the door to a number of intriguing future directions. First, since it is only limited by the operator light-cone, butterfly metrology represents the fastest way to generate metrologically-useful entanglement in any given interaction geometry [44]. For example, compared to recent work leveraging continuous symmetry breaking in two-dimensional dipoles [37, 71], butterfly metrology offers a quadratic speed-up to achieve the same enhanced sensitivity. Second, we note that achieving any sensitivity scaling beyond the standard quantum limit guarantees multi-partite entanglement [81]. Thus, from the perspective of entanglement verification [82], butterfly metrology provides a generic strategy for witnessing the entanglement generated by many-body quench dynamics. Finally, although we have focused on analog Hamiltonian dynamics, we note that butterfly metrology can also be realized using digital quantum circuits. In this setting, our protocol's robustness to coherent errors could be particularly advantageous for mitigating the effects of low-frequency noise and imperfect gate calibration [74, 83].

Acknowledgements—We gratefully acknowledge the insights of and discussions with Monika Schleier-Smith, Dan Stamper-Kurn, Francisco Machado, Antoine Browaeys, Marcus Bintz, Bingtian Ye, and Zilin Wang. This work was supported in part by multiple grants from the ARO (MURI program grant no. W911NF-20-1-0136 and grant no. W911NF-21-1-0262), and the Brown Institute for Basic Sciences. T.S. acknowledges support from the Walter Burke Institute for Theoretical Physics at Caltech. N.Y.Y. acknowledges support from a Simons Investigator award.

* These authors contributed equally to this work.

[1] V. Giovannetti, S. Lloyd, and L. Maccone, Quantum metrology, Physical review letters **96**, 010401 (2006).

- [2] L. Pezze, A. Smerzi, M. K. Oberthaler, R. Schmied, and P. Treutlein, Quantum metrology with nonclassical states of atomic ensembles, *Reviews of Modern Physics* **90**, 035005 (2018).
- [3] V. Giovannetti, S. Lloyd, and L. Maccone, Advances in quantum metrology, *Nature photonics* **5**, 222 (2011).
- [4] C. L. Degen, F. Reinhard, and P. Cappellaro, Quantum sensing, *Reviews of modern physics* **89**, 035002 (2017).
- [5] J. M. Robinson, M. Miklos, Y. M. Tso, C. J. Kennedy, T. Bothwell, D. Kedar, J. K. Thompson, and J. Ye, Direct comparison of two spin-squeezed optical clock ensembles at the 10- 17 level, *Nature Physics* **20**, 208 (2024).
- [6] A. L. Shaw, R. Finkelstein, R. B.-S. Tsai, P. Scholl, T. H. Yoon, J. Choi, and M. Endres, Multi-ensemble metrology by programming local rotations with atom movements, *Nature Physics* , 1 (2024).
- [7] P. Komar, E. M. Kessler, M. Bishof, L. Jiang, A. S. Sørensen, J. Ye, and M. D. Lukin, A quantum network of clocks, *Nature Physics* **10**, 582 (2014).
- [8] R. Schnabel, N. Mavalvala, D. E. McClelland, and P. K. Lam, Quantum metrology for gravitational wave astronomy, *Nature communications* **1**, 121 (2010).
- [9] J. Aasi, J. Abadie, B. Abbott, R. Abbott, T. Abbott, M. Abernathy, C. Adams, T. Adams, P. Addesso, R. Adhikari, *et al.*, Enhanced sensitivity of the ligo gravitational wave detector by using squeezed states of light, *Nature Photonics* **7**, 613 (2013).
- [10] M. e. Tse, H. Yu, N. Kijbunchoo, A. Fernandez-Galiana, P. Dupej, L. Barsotti, C. Blair, D. Brown, S. Dwyer, A. Effler, *et al.*, Quantum-enhanced advanced ligo detectors in the era of gravitational-wave astronomy, *Physical Review Letters* **123**, 231107 (2019).
- [11] G. Kucsko, P. C. Maurer, N. Y. Yao, M. Kubo, H. J. Noh, P. K. Lo, H. Park, and M. D. Lukin, Nanometre-scale thermometry in a living cell, *Nature* **500**, 54 (2013).
- [12] Y. Wu, F. Jelezko, M. B. Plenio, and T. Weil, Diamond quantum devices in biology, *Angewandte Chemie International Edition* **55**, 6586 (2016).
- [13] S. Bakhshandeh, Quantum sensing goes bio, *Nature Reviews Materials* **7**, 254 (2022).
- [14] N. Aslam, H. Zhou, E. K. Urbach, M. J. Turner, R. L. Walsworth, M. D. Lukin, and H. Park, Quantum sensors for biomedical applications, *Nature Reviews Physics* **5**, 157 (2023).
- [15] R. Bradley, J. Clarke, D. Kinion, L. J. Rosenberg, K. van Bibber, S. Matsuki, M. Mück, and P. Sikivie, Microwave cavity searches for dark-matter axions, *Reviews of Modern Physics* **75**, 777 (2003).
- [16] H. Zheng, M. Silveri, R. Brierley, S. Girvin, and K. Lehnert, Accelerating dark-matter axion searches with quantum measurement technology, *arXiv preprint arXiv:1607.02529* (2016).
- [17] D. Aybas, J. Adam, E. Blumenthal, A. V. Gramolin, D. Johnson, A. Kleyheeg, S. Afach, J. W. Blanchard, G. P. Centers, A. Garcon, *et al.*, Search for axionlike dark matter using solid-state nuclear magnetic resonance, *Physical Review Letters* **126**, 141802 (2021).
- [18] K. Lehnert, Quantum enhanced metrology in the search for fundamental physical phenomena, *SciPost Physics Lecture Notes* , 040 (2022).
- [19] G. Tóth and I. Apellaniz, Quantum metrology from a quantum information science perspective, *Journal of Physics A: Mathematical and Theoretical* **47**, 424006 (2014).
- [20] X.-M. Lu, S. Yu, and C. Oh, Robust quantum metrological schemes based on protection of quantum fisher information, *Nature communications* **6**, 7282 (2015).
- [21] F. Fröwis, P. Sekatski, and W. Dür, Detecting large quantum fisher information with finite measurement precision, *Physical review letters* **116**, 090801 (2016).
- [22] J. Liu, H. Yuan, X.-M. Lu, and X. Wang, Quantum fisher information matrix and multiparameter estimation, *Journal of Physics A: Mathematical and Theoretical* **53**, 023001 (2020).
- [23] G. Agarwal and L. Davidovich, Quantifying quantum-amplified metrology via fisher information, *Physical Review Research* **4**, L012014 (2022).
- [24] J. G. Bohnet, K. C. Cox, M. A. Norcia, J. M. Weiner, Z. Chen, and J. K. Thompson, Reduced spin measurement back-action for a phase sensitivity ten times beyond the standard quantum limit, *Nature Photonics* **8**, 731 (2014).
- [25] H. Zhang, R. McConnell, S. Čuk, Q. Lin, M. H. Schleier-Smith, I. D. Leroux, and V. Vuletić, Collective state measurement of mesoscopic ensembles with single-atom resolution, *Physical review letters* **109**, 133603 (2012).
- [26] G. Goldstein, P. Cappellaro, J. R. Maze, J. Hodges, L. Jiang, A. S. Sørensen, and M. Lukin, Environment-assisted precision measurement, *Physical review letters* **106**, 140502 (2011).
- [27] E. Davis, G. Bentsen, and M. Schleier-Smith, Approaching the heisenberg limit without single-particle detection, *Physical review letters* **116**, 053601 (2016).
- [28] T. Macrì, A. Smerzi, and L. Pezzè, Loschmidt echo for quantum metrology, *Physical Review A* **94**, 010102 (2016).
- [29] S. Colombo, E. Pedrozo-Peñafiel, A. F. Adiyatullin, Z. Li, E. Mendez, C. Shu, and V. Vuletić, Time-reversal-based quantum metrology with many-body entangled states, *Nature Physics* **18**, 925 (2022).
- [30] G. J. Mooney, G. A. White, C. D. Hill, and L. C. Hollenberg, Generation and verification of 27-qubit greenberger-horne-zeilinger states in a superconducting quantum computer, *Journal of Physics Communications* **5**, 095004 (2021).
- [31] M. Kitagawa and M. Ueda, Squeezed spin states, *Physical Review A* **47**, 5138 (1993).
- [32] I. D. Leroux, M. H. Schleier-Smith, and V. Vuletić, Implementation of cavity squeezing of a collective atomic spin, *Physical Review Letters* **104**, 073602 (2010).
- [33] R. J. Lewis-Swan, M. A. Norcia, J. R. Cline, J. K. Thompson, and A. M. Rey, Robust spin squeezing via photon-mediated interactions on an optical clock transition, *Physical review letters* **121**, 070403 (2018).
- [34] Y.-Q. Zou, L.-N. Wu, Q. Liu, X.-Y. Luo, S.-F. Guo, J.-H. Cao, M. K. Tey, and L. You, Beating the classical precision limit with spin-1 dicke states of more than 10,000 atoms, *Proceedings of the National Academy of Sciences* **115**, 6381 (2018).
- [35] X.-Y. Luo, Y.-Q. Zou, L.-N. Wu, Q. Liu, M.-F. Han, M. K. Tey, and L. You, Deterministic entanglement generation from driving through quantum phase transitions, *Science* **355**, 620 (2017).
- [36] B. Lücke, M. Scherer, J. Kruse, L. Pezzé, F. Deuretzbacher, P. Hyllus, O. Topic, J. Peise, W. Ertmer, J. Arlt, *et al.*, Twin matter waves for interferometry beyond the classical limit, *Science* **334**, 773 (2011).

- [37] M. Block, B. Ye, B. Roberts, S. Chern, W. Wu, Z. Wang, L. Pollet, E. J. Davis, B. I. Halperin, and N. Y. Yao, A universal theory of spin squeezing, arXiv preprint arXiv:2301.09636 (2023).
- [38] P. Hyllus, O. Gühne, and A. Smerzi, Not all pure entangled states are useful for sub-shot-noise interferometry, *Physical Review A* **82**, 012337 (2010).
- [39] D. A. Abanin, E. Altman, I. Bloch, and M. Serbyn, Colloquium: Many-body localization, thermalization, and entanglement, *Reviews of Modern Physics* **91**, 021001 (2019).
- [40] We remark that prior work introducing a connection between quantum-enhanced sensing and information scrambling relied on a non-standard OTOC involving a highly non-local operator [84]. Such OTOCs display substantially different physics than standard probes of scrambling. Correspondingly, the protocol in Ref. [84] will not succeed for generic many-body Hamiltonians, even if they scramble.
- [41] A. Kitaev, A simple model of quantum holography (2015).
- [42] S. H. Shenker and D. Stanford, Black holes and the butterfly effect, *Journal of High Energy Physics* **2014**, 1 (2014).
- [43] D. A. Roberts, D. Stanford, and L. Susskind, Localized shocks, *Journal of High Energy Physics* **2015**, 1 (2015).
- [44] Please see Supplemental Material for additional details..
- [45] D. D. Awschalom, R. Hanson, J. Wrachtrup, and B. B. Zhou, Quantum technologies with optically interfaced solid-state spins, *Nature Photonics* **12**, 516 (2018).
- [46] J. M. Taylor, P. Cappellaro, L. Childress, L. Jiang, D. Budker, P. Hemmer, A. Yacoby, R. Walsworth, and M. Lukin, High-sensitivity diamond magnetometer with nanoscale resolution, *Nature Physics* **4**, 810 (2008).
- [47] S. Castelletto, C. Lew, W.-X. Lin, and J.-S. Xu, Quantum systems in silicon carbide for sensing applications, *Reports on Progress in Physics* (2023).
- [48] S. L. Braunstein and C. M. Caves, Statistical distance and the geometry of quantum states, *Physical Review Letters* **72**, 3439 (1994).
- [49] For spin-1/2 particles, we adopt the convention that $|0\rangle$ is the “spin up” state, and $|1\rangle$ is the “spin down” state; i.e., $\sigma_z |0\rangle = |0\rangle$ and $\sigma_z |1\rangle = -|1\rangle$.
- [50] D. Bouwmeester, J.-W. Pan, M. Daniell, H. Weinfurter, and A. Zeilinger, Observation of three-photon greenberger-horne-zeilinger entanglement, *Physical Review Letters* **82**, 1345 (1999).
- [51] We note that the quantum circuit implementing this approach [i.e. Fig. 1(a)] is closely related to the one-sided implementation of the teleportation circuit shown in Ref. [54].
- [52] K. A. Landsman, C. Figgatt, T. Schuster, N. M. Linke, B. Yoshida, N. Y. Yao, and C. Monroe, Verified quantum information scrambling, *Nature* **567**, 61 (2019).
- [53] M. S. Blok, V. V. Ramasesh, T. Schuster, K. O’Brien, J.-M. Kreikebaum, D. Dahlen, A. Morvan, B. Yoshida, N. Y. Yao, and I. Siddiqi, Quantum information scrambling on a superconducting qutrit processor, *Physical Review X* **11**, 021010 (2021).
- [54] T. Schuster, B. Kobrin, P. Gao, I. Cong, E. T. Khabiboulline, N. M. Linke, M. D. Lukin, C. Monroe, B. Yoshida, and N. Y. Yao, Many-body quantum teleportation via operator spreading in the traversable wormhole protocol, *Physical Review X* **12**, 031013 (2022).
- [55] T. Zhou and B. Swingle, Operator growth from global out-of-time-order correlators, *Nature communications* **14**, 3411 (2023).
- [56] J. Maldacena, S. H. Shenker, and D. Stanford, A bound on chaos, *Journal of High Energy Physics* **2016**, 1 (2016).
- [57] Y. Sekino and L. Susskind, Fast scramblers, *Journal of High Energy Physics* **2008**, 065 (2008).
- [58] D. Hume, I. Stroescu, M. Joos, W. Muessel, H. Strobel, and M. Oberthaler, Accurate atom counting in mesoscopic ensembles, *Physical review letters* **111**, 253001 (2013).
- [59] M. W. Doherty, N. B. Manson, P. Delaney, F. Jelezko, J. Wrachtrup, and L. C. Hollenberg, The nitrogen-vacancy colour centre in diamond, *Physics Reports* **528**, 1 (2013).
- [60] A. Cooper, W. K. C. Sun, J.-C. Jaskula, and P. Cappellaro, Environment-assisted quantum-enhanced sensing with electronic spins in diamond, *Physical Review Applied* **12**, 044047 (2019).
- [61] M. Degen, S. Loenen, H. Bartling, C. Bradley, A. Meinsma, M. Markham, D. Twitchen, and T. Taminau, Entanglement of dark electron-nuclear spin defects in diamond, *Nature Communications* **12**, 3470 (2021).
- [62] R. Schirhagl, K. Chang, M. Loretz, and C. L. Degen, Nitrogen-vacancy centers in diamond: nanoscale sensors for physics and biology, *Annual review of physical chemistry* **65**, 83 (2014).
- [63] J. F. Barry, M. J. Turner, J. M. Schloss, D. R. Glenn, Y. Song, M. D. Lukin, H. Park, and R. L. Walsworth, Optical magnetic detection of single-neuron action potentials using quantum defects in diamond, *Proceedings of the National Academy of Sciences* **113**, 14133 (2016).
- [64] Y. Schlüssel, T. Lenz, D. Rohner, Y. Bar-Haim, L. Bougas, D. Groswasser, M. Kieschnick, E. Rozenberg, L. Thiel, A. Waxman, *et al.*, Wide-field imaging of superconductor vortices with electron spins in diamond, *Physical Review Applied* **10**, 034032 (2018).
- [65] L. Hall, P. Kehayias, D. Simpson, A. Jarmola, A. Stacey, D. Budker, and L. Hollenberg, Detection of nanoscale electron spin resonance spectra demonstrated using nitrogen-vacancy centre probes in diamond, *Nature communications* **7**, 10211 (2016).
- [66] C. Zu, F. Machado, B. Ye, S. Choi, B. Kobrin, T. Mittiga, S. Hsieh, P. Bhattacharyya, M. Markham, D. Twitchen, *et al.*, Emergent hydrodynamics in a strongly interacting dipolar spin ensemble, *Nature* **597**, 45 (2021).
- [67] J. Choi, H. Zhou, H. S. Knowles, R. Landig, S. Choi, and M. D. Lukin, Robust dynamic hamiltonian engineering of many-body spin systems, *Physical Review X* **10**, 031002 (2020).
- [68] C. Belthangady, N. Bar-Gill, L. M. Pham, K. Arai, D. Le Sage, P. Cappellaro, and R. L. Walsworth, Dressed-state resonant coupling between bright and dark spins in diamond, *Physical review letters* **110**, 157601 (2013).
- [69] G. Kucsko, S. Choi, J. Choi, P. C. Maurer, H. Zhou, R. Landig, H. Sumiya, S. Onoda, J. Isoya, F. Jelezko, *et al.*, Critical thermalization of a disordered dipolar spin system in diamond, *Physical review letters* **121**, 023601 (2018).
- [70] G. De Lange, Z. Wang, D. Riste, V. Dobrovitski, and R. Hanson, Universal dynamical decoupling of a single solid-state spin from a spin bath, *Science* **330**, 60 (2010).
- [71] C. Chen, G. Bornet, M. Bintz, G. Emperauger,

- L. Leclerc, V. S. Liu, P. Scholl, D. Barredo, J. Hauschild, S. Chatterjee, *et al.*, Continuous symmetry breaking in a two-dimensional rydberg array, *Nature* **616**, 691 (2023).
- [72] A. Periwal, E. S. Cooper, P. Kunkel, J. F. Wienand, E. J. Davis, and M. Schleier-Smith, Programmable interactions and emergent geometry in an array of atom clouds, *Nature* **600**, 630 (2021).
- [73] J. Braumüller, A. H. Karamlou, Y. Yanay, B. Kannan, D. Kim, M. Kjaergaard, A. Melville, B. M. Niedzielski, Y. Sung, A. Vepsäläinen, *et al.*, Probing quantum information propagation with out-of-time-ordered correlators, *Nature Physics* **18**, 172 (2022).
- [74] I. Pogorelov, T. Feldker, C. D. Marciniak, L. Postler, G. Jacob, O. Krieglsteiner, V. Podlesnic, M. Meth, V. Negnevitsky, M. Stadler, *et al.*, Compact ion-trap quantum computing demonstrator, *PRX Quantum* **2**, 020343 (2021).
- [75] L. Egan, D. M. Debroy, C. Noel, A. Risinger, D. Zhu, D. Biswas, M. Newman, M. Li, K. R. Brown, M. Cetina, *et al.*, Fault-tolerant control of an error-corrected qubit, *Nature* **598**, 281 (2021).
- [76] X. Chen and T. Zhou, Quantum chaos dynamics in long-range power law interaction systems, *Physical Review B* **100**, 064305 (2019).
- [77] T. Zhou, S. Xu, X. Chen, A. Guo, and B. Swingle, Operator lévy flight: Light cones in chaotic long-range interacting systems, *Physical review letters* **124**, 180601 (2020).
- [78] For the global protocol, we plot the metrological gain, instead of the sensitivity, since the global protocol has a sensitivity given by the SQL at time zero.
- [79] We note that this suppression factor is precisely the square of the so-called Loschmidt echo [80].
- [80] T. Schuster and N. Y. Yao, Operator growth in open quantum systems, *Physical Review Letters* **131**, 160402 (2023).
- [81] P. Hyllus, W. Laskowski, R. Krischek, C. Schwemmer, W. Wieczorek, H. Weinfurter, L. Pezzé, and A. Smerzi, Fisher information and multiparticle entanglement, *Physical Review A* **85**, 022321 (2012).
- [82] O. Gühne and G. Tóth, Entanglement detection, *Physics Reports* **474**, 1 (2009).
- [83] S. Krinner, S. Lazar, A. Remm, C. K. Andersen, N. Lacroix, G. J. Norris, C. Hellings, M. Gabureac, C. Eichler, and A. Wallraff, Benchmarking coherent errors in controlled-phase gates due to spectator qubits, *Physical Review Applied* **14**, 024042 (2020).
- [84] Z. Li, S. Colombo, C. Shu, G. Velez, S. Pilatowsky-Cameo, R. Schmied, S. Choi, M. Lukin, E. Pedrozo-Peñañiel, and V. Vuletić, Improving metrology with quantum scrambling, *Science* **380**, 1381 (2023).

Supplemental Material: A Universal Protocol for Quantum-Enhanced Sensing via Information Scrambling

Bryce Kobrin,^{1,*} Thomas Schuster,^{2,1,*} Maxwell Block,³ Weijie Wu,³ Bradley Mitchell,⁴ Emily Davis,^{3,5} and Norman Y. Yao³

¹*Department of Physics, University of California Berkeley, Berkeley, CA 94720, USA*

²*Walter Burke Institute for Theoretical Physics and Institute for Quantum Information and Matter, California Institute of Technology, Pasadena, CA 91125 USA*

³*Department of Physics, Harvard University, Cambridge, MA 02138, USA*

⁴*IBM Quantum, IBM Almaden Research Center, San Jose, CA 95120, USA*

⁵*Department of Physics, New York University, New York, NY, 10003, USA*

(Dated: November 21, 2024)

CONTENTS

| | |
|--|----|
| I. Comparison to existing time-reversed sensing protocols | 1 |
| II. Detailed analysis of the sensitivity | 3 |
| A. Butterfly metrology with local control | 3 |
| B. Butterfly metrology with global control | 4 |
| III. Experimental proposals | 5 |
| A. Dipolar Rydberg atoms | 6 |
| B. Hybrid spin system in diamond | 6 |
| C. Ensemble of NV centers in diamond | 9 |
| D. Atoms in an optical cavity | 10 |
| E. Superconducting qubits with analog interactions | 10 |
| F. Trapped-ion quantum computer | 11 |
| IV. Details on stochastic model used for large-scale numerical studies | 11 |
| V. Detailed analysis of the effects of noise and decoherence | 13 |
| VI. Experimental protocol to measure the opposite quadrature | 16 |
| References | 17 |

I. COMPARISON TO EXISTING TIME-REVERSED SENSING PROTOCOLS

Many of the most prominent protocols for quantum-enhanced sensing involve the use of time-reversed dynamics, through variants of the so-called echo protocol [1–4] (depicted in Fig. S1). These protocols all feature a crucial difference from our proposed butterfly metrology protocol, in that they utilize only a *single step each* of forward and reverse time evolution. Namely, the metrological state is prepared via forward evolution from a product state, $U|\mathbf{0}\rangle$, and reverse evolution is applied solely to assist readout. As a result, such protocols can only achieve a quantum enhancement for extremely specific classes of unitary dynamics, i.e. those that generate a large quantum Fisher information (QFI) when applied to a product state. In contrast, butterfly metrology utilizes a combination of forward and reverse time evolution to *prepare* a metrologically-useful state; as we show in our work, this enables a Heisenberg-scaling quantum enhancement for completely generic interacting dynamics.

* These authors contributed equally to this work.

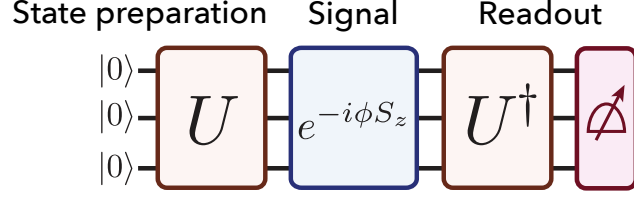


FIG. S1. Schematic depiction of existing time-reversal-based protocols for quantum-enhanced sensing [1–4]. Forward time evolution is used to prepare the metrological state, and reverse evolution is applied solely during readout.

To illustrate this distinction, let us recall a few classes of unitaries U for which the standard echo protocol has previously been applied. First, take U to be a Clifford circuit that prepares a GHZ state, i.e. $U|\mathbf{0}\rangle = (|0\rangle^{\otimes N} + |1\rangle^{\otimes N})/\sqrt{2}$. The full sensing scheme consists of applying U to generate a GHZ state, accumulating a phase under the external signal, and then applying the inverse preparation circuit to refocus the acquired phase to a single-body observable. This last step is not strictly necessary—one could instead readout the signal via global parity measurements of the GHZ state; however, readout via a local observable provides a practical advantage as it leads to much greater robustness to readout noise^a[3]. Second, take $U = e^{-iHt}$ to be time evolution under a large-spin Hamiltonian, e.g. the one-axis twisting model, $H = S_z^2$ with $S_z = \frac{1}{2} \sum_i \sigma_i^z$. Such Hamiltonians are governed by effectively semi-classical dynamics owing to the large-spin degree of freedom. These dynamics can be used to generate metrological spin-squeezed states from solely forward time evolution [1, 4]. Much like for the GHZ state, the effect of the signal can in principle be detected directly, via measurements on the squeezed state; however, in practice, applying the inverse preparation, $U^\dagger = e^{iHt}$, to “un-squeeze” the state substantially improves the robustness to readout noise [1, 5]. Additional examples of unitary dynamics proposed for the echo protocol include time evolution under certain integrable Hamiltonians [6] or Hamiltonians that feature a continuous-symmetry-breaking phase [7].

Crucially, however, the echo protocol shown in Fig. S1 *does not* lead to any metrological enhancement for generic interacting quantum dynamics, outside of these few, highly specific cases. To illustrate this limitation in a simple example, consider when U is taken to be a Haar-random unitary. This serves as a standard model for the late-time dynamics of generic interacting quantum systems. In this case, the state prepared under forward evolution, $U|\mathbf{0}\rangle$ is a Haar-random state. A Haar-random state has an average Fisher information

$$\begin{aligned} \mathbb{E}_\psi [\mathcal{F}] &= 2\mathbb{E}_\psi \left[\langle \psi | S_z^2 | \psi \rangle - \langle \psi | S_z | \psi \rangle^2 \right] \\ &= \frac{1}{2^N} \text{tr}(S_z^2) - \frac{1}{2^N(2^N + 1)} \left(\text{tr}(S_z)^2 + \text{tr}(S_z^2) \right) \\ &= \frac{N}{4} + \mathcal{O}\left(\frac{N}{2^N}\right), \end{aligned} \quad (1)$$

which implies a sensitivity that is bounded by the standard quantum limit. Intuitively, this follows because a random state, with high probability, has no long-range correlations in the z -basis.

As discussed in the main text and shown in detail below, our protocol circumvents this restriction, enabling Heisenberg-scaling sensitivities for any generic interacting Hamiltonian dynamics. This greater versatility opens the door to achieving a metrological enhancement in a much wider variety of experimental platforms (e.g. the spin systems discussed in Sections III B and III C). Furthermore, even in systems that can achieve a metrological enhancement using existing echo protocols, our approach can offer several advantages with respect to the preparation time, and robustness to coherent errors, as discussed further in Sections III E and III F.

^a Interestingly, sensing with a GHZ state can be understood as a special case of our protocol. Consider a protocol which prepares the GHZ state by applying a $\pi/2$ -pulse to the first qubit, $(\mathbb{1} + i\sigma_0^x)/\sqrt{2}$, followed by a CNOT “ladder” denoted U . To detect the accumulated phase from an external signal, the inverse ladder U^\dagger is applied and the first qubit is measured. The final state (up to normalization) is $U^\dagger e^{i\phi S_z} U(\mathbb{1} + i\sigma_0^x)|\mathbf{0}\rangle$. Because $|\mathbf{0}\rangle$ is an eigenstate of the CNOT gates, we can insert an additional copy of U^\dagger at the beginning of the circuit without changing the final outcome: $U^\dagger e^{i\phi S_z} U(\mathbb{1} + i\sigma_0^x)U^\dagger|\mathbf{0}\rangle$. This is precisely of the form of our protocol, upon swapping $U \leftrightarrow U^\dagger$.

II. DETAILED ANALYSIS OF THE SENSITIVITY

Here, we provide further details on our calculations of the sensitivity of both the local and global variants of butterfly metrology.

A. Butterfly metrology with local control

We begin with the local protocol. As discussed in the main text, the signal of the local protocol takes the following form,

$$\begin{aligned} \langle V \rangle_\phi &= \frac{1}{2} \langle \mathbf{0} | V(t) | \mathbf{0} \rangle - \frac{1}{2} \langle \mathbf{0} | V(t) e^{i\phi S_z} V(t) e^{-i\phi S_z} V(t) | \mathbf{0} \rangle \\ &\quad + \text{Im} \left[e^{i\phi N/2} \langle \mathbf{0} | V(t) e^{-i\phi S_z} V(t) | \mathbf{0} \rangle \right]. \end{aligned} \quad (2)$$

where V is a Pauli operator and $V(t) = U^\dagger V U$. At late times, we approximate the evolution e^{-iHt} by a Haar-random unitary U . For such a unitary, the first two terms in the signal vanish in expectation, leaving only the final term non-zero. To analyze this term, we decomposed the perturbed state in the computational basis as $V(t) | \mathbf{0} \rangle = \sum_{s \in \{0,1\}^N} c_s |s\rangle$, and define the *polarization distribution* $P(S_z) = \sum_{|s|=2S_z} |c_s|^2$, where $|s| = \sum_i (-1)^{s_i}$ and $S_z = -N/2, -N/2 + 1, \dots, N/2 - 1, N/2$. We observe that the signal is determined by the characteristic function of the distribution,

$$\langle V \rangle_\phi = \text{Im} \left[e^{i\phi N/2} \sum_{S_z=-N/2}^{N/2} e^{-i\phi S_z} P(S_z) \right] \quad (3)$$

$$= \text{Im} \left[e^{i\phi N/2} \Phi(\phi) \right] \quad (4)$$

where $\Phi(\phi) = \sum_{S_z=-N/2}^{N/2} e^{-i\phi S_z} P(S_z)$. Since U is a Haar-random unitary, we can approximate the perturbed state as a Haar-random state. This leads to a binomial polarization distribution, $P(S_z) = \frac{1}{2^N} \binom{N}{N/2-S_z}$. Plugging this distribution into Eq. (3) allows us to compute the expected signal as a function of ϕ , as shown in Fig. 2(b) of the main text.

To analyze the sensitivity for small values of ϕ , we Taylor expand Eq. (3) to leading order. The sensitivity is determined by the first moment of $P(S_z)$,

$$\eta_{\phi=0}^{-1} = N/2 - \sum_{S_z} S_z P(S_z). \quad (5)$$

The polarization distribution for a Haar-random unitary has mean zero and thus leads to $\eta_{\phi=0} = 2/N$, a factor of 2 above the strict Heisenberg limit.

For larger ϕ , two effects that cause the sensitivity to deviate from this maximal value. The first effect is not particularly important, and arises simply because our signal, $\langle V \rangle_\phi$, is oscillatory as a function of ϕ . This causes the sensitivity to similarly oscillate between zero and its maximal value. If desired, this effect can easily be mitigated by measuring the opposite quadrature of the oscillation (i.e. measuring the real part of the characteristic function, $\text{Re} [e^{i\phi N/2} \Phi(\phi)]$, in addition to the imaginary part); we provide an explicit protocol to do so in Section VI. The optimal sensitivity is obtained by taking a linear combination of the real and imaginary parts, $C(\phi, \theta) = \cos(\theta) \text{Re} [e^{i\phi N/2} \Phi(\phi)] + \sin(\theta) \text{Im} [e^{i\phi N/2} \Phi(\phi)]$, and maximizing $|\partial_\phi C(\phi, \theta)|$ with respect to θ . This yields an optimal sensitivity $\eta_\phi^{-1} = |-iN/2\Phi(\phi) + \Phi'(\phi)|$.

The second effect of a larger ϕ is more fundamental, and arises due to the finite width of the polarization distribution, $P(S_z)$, about its mean value [see e.g. Fig. 2(a) of the main text]. Intuitively, this non-zero width causes the magnitude of the expectation value, $\langle \mathbf{0} | V(t) e^{-i\phi S_z} V(t) | \mathbf{0} \rangle$, to decrease below unity, since the state, $V(t) | \mathbf{0} \rangle$, is no longer a perfect eigenstate of $e^{-i\phi S_z}$. This damps the sensitivity by a factor of, roughly,

$$|\langle \mathbf{0} | V(t) e^{-i\phi S_z} V(t) | \mathbf{0} \rangle| \approx 1 - \frac{1}{2} \phi^2 \left(\langle \mathbf{0} | V(t) S_z^2 V(t) | \mathbf{0} \rangle - \langle \mathbf{0} | V(t) S_z V(t) | \mathbf{0} \rangle^2 \right) \quad (6)$$

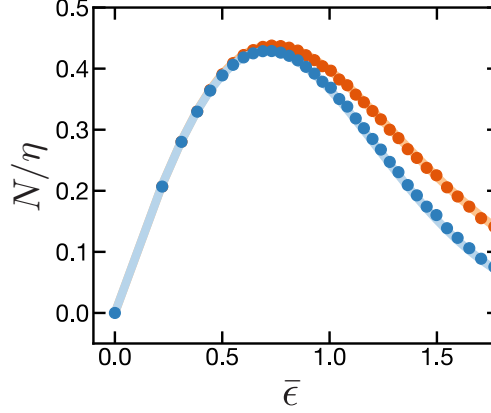


FIG. S2. The sensitivity of butterfly metrology with global controls as a function of the re-scaled preparation angle, $\bar{\epsilon} = \sqrt{N}\epsilon/2$, for the measurement operator S_x (blue), and the measurement operator $\sin(\epsilon S_x)$ (orange). We observe excellent agreement between the analytic prediction for Haar-random evolution (solid line) and the late-time dynamics of an interacting Hamiltonian on $N = 18$ spins (points). In this plot, the spin Hamiltonian consists of all-to-all two-body interactions with random magnitudes, $H = \sum_{i < j} \sum_{\mu, \nu} J_{ij}^{\mu\nu} \sigma_\mu^i \sigma_\nu^j$, where $\mu, \nu \in \{X, Y, Z\}$ and $J_{ij}^{\mu\nu}$ are Gaussian random numbers with mean zero and standard deviation J/\sqrt{N} . The evolution time is $tJ = 10$. Similar results are obtained for generic Hamiltonians, including translation-invariant Hamiltonians in 1D and 2D, although the agreement between such Hamiltonians and the Haar-random prediction is not as precise as above at the accessible system sizes.

where on the RHS we Taylor expand to second order in ϕ . The damping is controlled by ϕ^2 multiplied by the variance of the polarization distribution. In a Haar-random state, the polarization distribution has variance $\sim N$, which leads the sensitivity to decay from its maximal value for $\phi \gtrsim 1/\sqrt{N}$. In Fig. 2 of the main text, we corroborate this prediction by plotting the exact sensitivity with respect to ϕ for a Haar-random unitary. As expected, we observe that the range for high sensitivity is $\phi \lesssim 1/\sqrt{N}$. In the limit $N \gg 1$, we can compute the full functional form of the sensitivity by approximating the polarization distribution as a Gaussian, $P(S_z) \approx e^{-2S_z^2/N}$, which yields a sensitivity $\eta_\phi^{-1} \approx (N/2)e^{-\phi^2 N/8}$.

B. Butterfly metrology with global control

We now turn to the global variant of butterfly metrology. The signal takes the form

$$\begin{aligned} \langle S_x \rangle_\phi &= a^2 \langle \mathbf{0} | S_x(t) | \mathbf{0} \rangle - \langle \mathbf{0} | \tilde{V}(t) e^{i\phi S_z} S_x(t) e^{-i\phi S_z} V(t) | \mathbf{0} \rangle \\ &\quad + 2a \text{Im} \left[e^{i\phi \frac{N}{2}} \langle \mathbf{0} | S_x(t) e^{-i\phi S_z} \tilde{V}(t) | \mathbf{0} \rangle \right], \end{aligned} \quad (7)$$

where we decompose the global rotation as $e^{i\epsilon S_x} \equiv a\mathbb{1} + i\tilde{V}$, where $a = \cos^N(\epsilon)$ and \tilde{V} is traceless, as described in the main text. We note two key differences between the signal, Eq. (7), of the global protocol, and the signal, Eq. (2), of the local protocol. First, the global protocol contains the free parameter, a , which is set by our choice of the rotation angle, ϵ . Second, the third term in the signal of the global protocol involves a matrix element between two *distinct* quantum states, $\tilde{V}(t) | \mathbf{0} \rangle$ and $S_x(t) | \mathbf{0} \rangle$.

Let us first address the behavior of the global protocol for late time, i.e. Haar-random evolution, and then turn to earlier times. Similar to the local protocol, when U is Haar-random only the third term in the signal is non-vanishing. Moreover, within the third term, only the component of $\tilde{V}(t) | \mathbf{0} \rangle$ that overlaps with $S_x(t) | \mathbf{0} \rangle$ contributes to the matrix element. In particular, if we decompose the global rotation as $e^{i\epsilon S_x} = a\mathbb{1} + i2a \tan(\epsilon/2) S_x + S_{x,\perp}$, where $\text{tr}(S_x S_{x,\perp}) = 0$, then the Haar average retains only the term proportional to S_x . Thus, the signal simplifies to

$$\langle S_x \rangle_\phi = 4a^2 \tan(\epsilon/2) \cdot \text{Im} \left[e^{-i\phi \frac{N}{2}} \langle \mathbf{0} | S_x(t) e^{i\phi S_z} S_x(t) | \mathbf{0} \rangle \right]. \quad (8)$$

We note that, crucially, the state $S_x(t) | \mathbf{0} \rangle$ has normalization $\langle \mathbf{0} | S_x(t) S_x(t) | \mathbf{0} \rangle = N/4$.

| Experimental platform | Form of interaction | Geometry | Control | Initial state | Mechanism for time reversal |
|-------------------------|---------------------|------------------|---------|---------------|-----------------------------|
| Dipolar Rydberg atoms | Dipolar XY | 1D or 2D | Either | Random | Rydberg-state encoding |
| Hybrid spin system | Dipolar Ising/XXZ | 3D with disorder | Local | Polarized | Hamiltonian engineering |
| Ensemble of NV centers | Dipolar XXZ | 3D with disorder | Global | Polarized | Hamiltonian engineering |
| Atoms in optical cavity | Long-range XY | Variable | Global | Polarized | Sign of laser detuning |
| Superconducting qubits | Local XY | 2D | Either | Random | Conjugation by pi-pulses |
| Trapped ions | Digital gates | Variable | Either | Either | Phase of laser excitation |

TABLE I. A more detailed overview of our proposed implementations of butterfly metrology in variety of experimental platforms. The range of interaction forms and system geometries demonstrates the versatility of butterfly metrology. For certain platforms, we observe that it is helpful to randomize the initial state in a fixed product basis, to avoid undesirable effects associated with the fact that the polarized state has very low energy under the system’s Hamiltonian.

Signal in hand, we now turn to the sensitivity, $\eta_{\phi=0}^{-1} \equiv (\partial_{\phi}\langle S \rangle_{\phi} / \Delta S_{\phi})_{\phi=0}$, of the global protocol. For convenience, we work in the limit $N \gg 1$, such that $a = \cos^N(\epsilon/2) \approx \exp(-\bar{\epsilon}^2/2)$, where $\epsilon \equiv 2\bar{\epsilon}/\sqrt{N}$ and $\bar{\epsilon}$ is an order-one constant. For small values of ϕ , we have $\partial_{\phi}\langle S_x \rangle_{\phi=0} \approx a^2\bar{\epsilon}N^{3/2}/2$. Meanwhile, the standard deviation of the global measurement is $\Delta S_{\phi=0} = \sqrt{N}/2$. This yields $\eta_{\phi=0}^{-1} \approx \bar{\epsilon}e^{-\bar{\epsilon}^2}N$, with an optimal value $\eta^{-1} = (1/\sqrt{2\bar{\epsilon}})N \approx 0.43N$ achieved at $\bar{\epsilon} = 1/\sqrt{2}$. In Fig. 4(b) of the main text, we compare this prediction to the sensitivities obtained in exact numerical simulations of a spin model with $N = 18$ spins and observe excellent agreement.

We remark that, interestingly, measuring the global spin operator, S_x , is in some cases not the optimal measurement for the global protocol. In particular, for Haar-random evolution, and a very small improvement in sensitivity may be achieved by instead computing the expectation value of the operator, $M = \tilde{V} + \tilde{V}^\dagger = 2\sin(\epsilon S_x)$. Deriving the sensitivity with respect to a measurement of M is straightforward but tedious, so we simply quote the result: $\eta_{\phi=0}^{-1} = (a/\sqrt{2})(1-a^4)^{1/2}N$, which yields an optimal sensitivity $\eta^{-1} = (1/3^{3/4})N \approx 0.44N$. Although this offers a minute advantage over the original protocol, it may be more challenging to realize experimentally since it involves measuring higher powers of S_x .

To understand the sensitivity of the global protocol at earlier times, we leverage the connection between butterfly metrology and operator growth introduced in detail in the main text. To begin our analysis, we note that the global rotation $e^{i\epsilon S_x}$ flips each spin in the system with probability $\sin^2(\epsilon/2) \sim \epsilon^2$. Thus, the perturbation \tilde{V} consists of $\sim \epsilon^2 N$ local spin operators at time zero, separated in space by a typical distance $\sim 1/\epsilon^2$ (working in 1D for simplicity). As we time evolve, each local operator grows to have support on a larger region of \mathcal{S} spins. For a given time, the sensitivity is optimized when we set $\epsilon \sim 1/\sqrt{\mathcal{S}}$, just small enough so that the operators remain separated after time evolution. In this regime, the global protocol factorizes, to good approximation, into N/\mathcal{S} parallel protocols on \mathcal{S} spins each. Now, suppose that we set the evolution time (or conversely, set ϵ) so that each local operator time evolves to have support on a region of size $\mathcal{S} \sim 1/\epsilon$. In this case, the typical behavior of the global protocol resembles that of $\sim N/\mathcal{S}$ copies of the *local* rotation protocol performed in parallel. Each “local” protocol is evolved to the scrambling time on \mathcal{S} spins, and thus has a Heisenberg-scaling sensitivity $\eta^{-1} \sim \mathcal{S}$. These add in quadrature to give a total sensitivity $\eta^{-1} \sim \sqrt{N\mathcal{S}}$. As we increase time, the size \mathcal{S} smoothly increases from 1 to N , yielding a sensitivity that smoothly improves from the SQL to the Heisenberg limit. The precise functional form of this interpolation will depend on the growth of the operator support \mathcal{S} under the specific Hamiltonian dynamics of interest; we refer to the main text for further discussion.

III. EXPERIMENTAL PROPOSALS

In this section, we present additional details on the two experimental platforms highlighted in the main text, along with four additional platforms that are amenable to implementing our protocol. A brief overview of these systems and our proposed implementations is provided in Table I.

Before discussing the systems individually, we note that a few features are in common in all of the proposals. First, we choose the initial state of the protocol to be quantized along the X direction. This is motivated by the fact that all of the systems (except the trapped ion quantum computer) feature native interactions that conserve total polarization in the Z basis. Specifically, we either consider a fully polarized state, or we

average over random initial states in the X basis. The latter approach allows us to circumvent low-energy effects associated with a polarized state; this is most relevant for the two systems with entirely ferromagnetic interactions, i.e. the dipolar Rydberg atoms and the superconducting qubits. Moreover, in all cases, we select a “butterfly” operator that lies the transverse plane (i.e. $V = \sigma_x$ or $S = S_x$). This generally leads to faster scrambling compared to an operator that overlaps with the conserved quantity S_z [8].

A. Dipolar Rydberg atoms

One particularly suitable platform for realizing our protocol—with either local or global controls—is a quantum simulator based on a 1D or 2D array of atoms trapped in optical tweezers [9, 10]. For each atom, an effective spin-1/2 degree of freedom is encoded in a pair of Rydberg states, which is governed by a long-range XY interaction:

$$H = -J \sum_{i < j} \frac{a^3}{r_{ij}^3} (\sigma_x^i \sigma_x^j + \sigma_y^i \sigma_y^j) \quad (9)$$

where $J \approx 1$ MHz is the dipolar interaction strength, $a \sim 10 \mu\text{m}$ is the lattice spacing, and r_{ij} is the distance between atoms. Crucially, the sign of J is controlled by the specific Rydberg state encoding; for example, $J > 0$ occurs for the encoding $|0\rangle = |60S_{1/2}, m = 1/2\rangle$ and $|1\rangle = |60P_{3/2}, m = -1/2\rangle$ [9, 11]. Switching between two encodings (via a microwave pulse) allows one to realize time-reversed dynamics. Furthermore, one can implement global rotations via microwave pulses and single-site rotations by applying a focused laser beams, which generates a local Stark shift. Such control is necessary to prepare a random initial state, as well as to apply the local rotation $e^{i\frac{\pi}{4}V}$ (for the local control protocol).

In Fig. S4(a), we present simulated results for the protocol with local controls with a 2D array of atoms. The initial state is randomized over product states in the X basis, and the butterfly operator is $V = \sigma_x^{N/2}$ (located in the center of the array). At early times, we observe a rapid improvement in sensitivity, which for a large system we would expect to follow a quadratic trend, i.e. $1/\eta \sim t^2$. At later times, the sensitivity abruptly saturates at $\eta \approx 2/N$, consistent with our prediction from Haar-random evolution and indicating that the system has fully scrambled.

In practice, the improvement in sensitivity over time would compete with the suppression due to accumulation of errors (see Section V for details). A leading source of decoherence in the system is the lifetime of the Rydberg state, which is typically $T_1 \sim 100 \mu\text{s}$ [12]. Based on an interaction strength of $J \sim 1$ MHz [9], we estimate this would enable a high-fidelity preparation of a fully scrambled state for $N \sim 25$ in 1D and $N \sim 100$ in 2D, corresponding to a metrological gain of 8 and 14 dB, respectively.

Interestingly, a recent work proposed also proposed the use of 2D Rydberg arrays for generating spin squeezed states [7]. This approach enables an enhanced sensitivity $N^{-7/10}$ after an evolution time $t \sim N^{2/5}$. With the same 2D array of atoms, we observe that our protocol could obtain a comparable sensitivity at a time $t \sim N^{1/5}$, i.e. representing a quadratic speedup. Moreover, the scaling difference between the two protocols is dependent on the dimensionality; whereas the scaling in our protocol improves for higher dimensions, spin-squeezing occurs with the same functional form for all dimensions [7]. For example, in 1D, the sensitivity for the two protocols would exhibit the same scaling in time, and, in 3D, our protocol would feature a cubic speedup. This highlights the fact that scrambling occurs at a near-maximal rate under many-body dynamics.

B. Hybrid spin system in diamond

As discussed in the main text, our protocol with local controls can naturally be realized in a bulk diamond sample containing two species of electronic spin defects: a relatively high concentration of spin-1/2 nitrogen substitutional defects (P1 centers), and a low density of spin-1 nitrogen-vacancy (NV) centers [13].

When the two species are off-resonant, the intrinsic magnetic dipole interaction between a single NV center

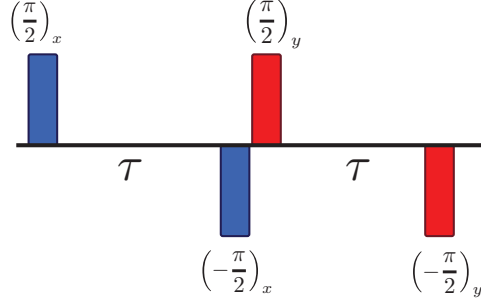


FIG. S3. A pulse sequence for engineering the hybrid spin Hamiltonian H [Eq. (10)] into \tilde{H}^+ [Eq. (14)]. The sequence consists of two frame rotations with equal duration, τ . In the first, a $\pi/2$ pulse applied along the X direction brings P_z into P_y and P_y into $-P_z$. In the second, a $\pi/2$ pulse applied along the Y direction brings P_z into P_x and P_x into $-P_z$. By rotating in the opposite direction (i.e. switching $\pi/2$ into $-\pi/2$ and vice versa), the pulse sequence instead generates \tilde{H}^- .

and the surrounding P1 centers gives rise to an effective Hamiltonian [13]

$$H = H_{NV-P1} + H_{P1-P1} \quad (10)$$

$$H_{NV-P1} = J_0 \sum_i \frac{1}{r_{ij}} (1 - 3n_{ij}^z) s_z p_z^i \quad (11)$$

$$H_{P1-P1} = -\frac{J_0}{2} \sum_{i < j} \frac{1}{r_{ij}} (1 - 3n_{ij}^z) (p_x^i p_x^j + p_y^i p_y^j - 2p_z^i p_z^j). \quad (12)$$

Here, $J_0 \approx 52$ MHz-nm³ is the magnetic dipole interaction; \vec{s}_i, \vec{p}_i^j are local spin-1/2 operators acting on the NV center (within the $|m=0\rangle$ and $|m=-1\rangle$ subspace) and individual P1 centers, respectively; r_{ij} is the distance between two defects; and $n_{ij}^z = \hat{z} \cdot \hat{r}_{ij}$.

The sign of H_{NV-P1} can easily be reversed by conjugating the evolution via a π -pulse on the NV center, leading to the effective Hamiltonian

$$H^- = -H_{NV-P1} + H_{P1-P1}. \quad (13)$$

To reverse the sign of H_{P1-P1} , we can apply global pulses to the P1 centers following the pulse sequence shown in Fig. S3. From average Hamiltonian theory, the engineered Hamiltonian in the toggling frame is

$$\tilde{H}^\pm = \pm \tilde{H}_{NV-P1} - \frac{1}{2} H_{P1-P1} \quad (14)$$

$$\tilde{H}_{NV-P1} = \frac{J_0}{2} \sum_i \frac{1}{r_{ij}} (1 - 3n_{ij}^z) s_z (p_x^i + p_y^i), \quad (15)$$

where the sign in front of \tilde{H}_{NV-P1} is determined by direction of the pulses (Fig. S3). Putting these pieces together, we can realize forward and reverse evolution under \tilde{H}^+ :

$$U = e^{-it\tilde{H}^+} \quad (16)$$

$$U^\dagger = e^{-i2t[\frac{1}{2}\tilde{H}^- + \frac{1}{4}(H+H^-)]} = e^{it\tilde{H}^+}. \quad (17)$$

The full protocol is thus implemented as follows:

1. Initialize in a fully polarized state in the Z direction. This is achieved for the NV centers via optical polarization and for the P1 centers via cryogenic conditions.
2. Rotate the state to the X direction by applying a microwave pulse resonant with (a) the two levels of the P1 center, and (b) the $|m_s=0\rangle \leftrightarrow |m_s=-1\rangle$ transition of the NV center.
3. Evolve under the engineered Hamiltonian \tilde{H}_+ by applying the pulse sequence described above.

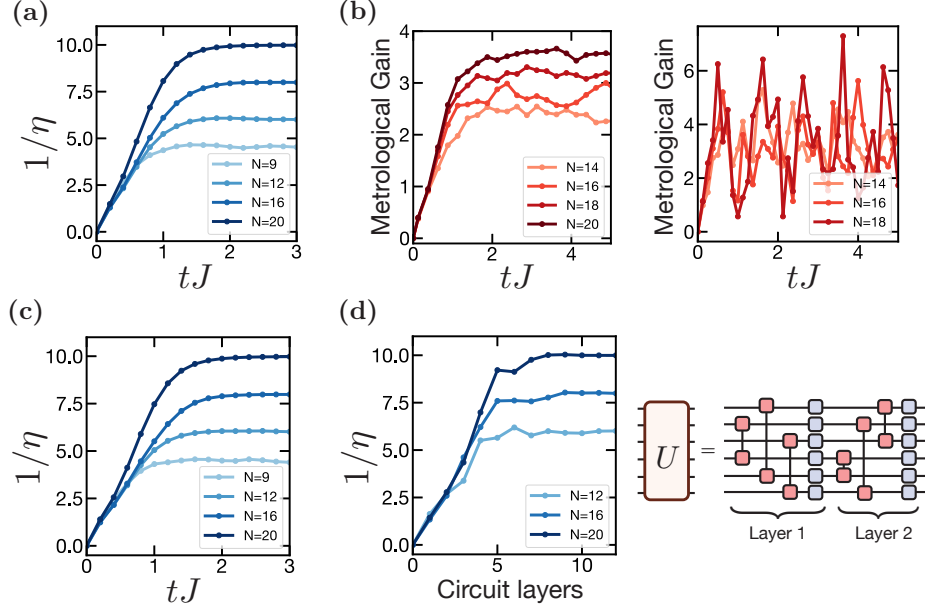


FIG. S4. Numerical simulations of our protocol with four proposed experimental platforms: (a) Rydberg dipolar atoms in two-dimensions, i.e. Eq. (9) with $r_{ij} = 1$ for nearest neighbors; (b) atoms in an optical cavity, i.e. Eq. (22-23), with (left) $s = -\frac{1}{2}$ and (right) $s = \frac{1}{2}$; (c) superconducting qubits with analog interactions, Eq. (24); (d) trapped ions under a non-local, random unitary circuit. In (a),(c), and (d), the protocol with local controls is performed and the initial state is a random product state in the X basis (averaged over ~ 10 realizations). In (b), we implement the protocol with global controls and a fully polarized state initial state, $|\mathbf{0}\rangle = |+\rangle^{\otimes N}$. The circuit geometry for the trapped ion simulations is shown in (d). Each layer consists of $N/2$ two-qubit gates (red), acting on random pairs of qubits, and a random single-qubit rotation on each of the qubits (blue).

4. Apply a local rotation to the NV and evolve backwards under $-\tilde{H}_+$. The steps up to this point produce the butterfly state.
5. Apply the global sensing signal $e^{-i\phi S_z}$, where $S_z = s_z + \sum_i p_z^i$.
6. Evolve forward again under \tilde{H}_+ , and measure the polarization of the NV center using optical excitation.

We emphasize that the protocol succeeds despite the presence of strong positional disorder in the spin system: Any position configurations would lead to many-body interactions which produce scrambling behavior and thus an enhancement in sensitivity^b. Moreover, as discussed in the main text, the scrambling occurs very fast—i.e. at super-polynomial rate—due to the long-range interactions in three dimensions. For comparison, a previous scheme has been proposed for entanglement-enhanced sensing with the NV-P1 hybrid system, in which the sensitivity improves linearly in time, i.e. $1/\eta \sim t$ [6].

A particularly attractive feature of electronic spins in diamond is their extremely long intrinsic lifetimes, e.g. $T_1 \sim$ seconds at low temperatures [14]. In most settings, the coherence times are instead determined by interactions with other spin defects (both electronic or nuclear spins). Fortunately, in our protocol, these interactions can be dynamically decoupled by interspersing the pulse sequences described above with global pi-pulses. As a result, we expect our protocol to be primarily limited by technical constraints, e.g. the ability to implement pulse sequences with high fidelity and at a pulse rate that is faster than the intrinsic interaction strengths. Recent work has led to significant improvements in the robustness of Hamiltonian engineering techniques, which can be leveraged to overcome some of these constraints [15].

^b In an ensemble of NV centers, each with their own P1 environment, the total sensitivity $\eta_{\phi=0}$ is given by the average sensitivity over the positional configurations contained in the ensemble.

C. Ensemble of NV centers in diamond

A second system of spin defects which can realize our protocol with *global control* is an ensemble of strongly interacting NV centers [16]. The main benefit of this implementation, compared with a hybrid NV-P1 system, is that NV centers can be optically polarized at room temperature, thereby circumventing the need for cryogenic temperatures.

As in the previous section, time reversal of the NV interactions can be realized by applying pulse engineering techniques. We first consider the effective interaction between NV centers within the two-level subspace $\{|0\rangle, |-1\rangle\}$ [16]:

$$H_0 = J_0 \sum_{i<j} \frac{1}{r_{ij}} (1 - 3n_{ij}^z) (s_x^i s_x^j + s_y^i s_y^j - s_z^i s_z^j), \quad (18)$$

where s^i are spin-1/2 operators acting in the two-level subspace. Unfortunately, this Hamiltonian *cannot* be time reversed using a sequence of frame rotations. This results from the observation that the matrix representation of the individual Hamiltonian terms—i.e. $h_{\mu\nu}$ where $H_{ij} = \sum_{\mu\nu} h_{\mu\nu} s_\mu^i s_\nu^j$ and $\mu, \nu \in \{X, Y, Z\}$ —has non-zero trace $\sum_\mu h_{\mu\mu}$, and global operations preserve the trace [15].

Nevertheless, the NV center contains another potential two-level subspace composed of the $m_s = \pm 1$ sublevels, wherein the effective interaction is

$$H_{\pm 1} = -4J_0 \sum_{i<j} \frac{1}{r_{ij}} (1 - 3n_{ij}^z) s_z^i s_z^j. \quad (19)$$

Because the trace of $H_{\pm 1}$ has the opposite sign as H_0 , one can combine the two subspaces to engineer an average Hamiltonian that is traceless. In particular, alternating between the two subspaces, with duration τ in the first subspace and duration $\tau/4$ in the second subspace, yields the effective Hamiltonian:

$$\tilde{H} = \frac{4}{5} \left(H_0 + \frac{1}{4} H_{\pm 1} \right) \quad (20)$$

$$= \frac{4J_0}{5} \sum_{i<j} \frac{1}{r_{ij}} (1 - 3n_{ij}^z) (s_x^i s_x^j + s_y^i s_y^j - 2s_z^i s_z^j). \quad (21)$$

This Hamiltonian is simply proportional to the dipolar interaction among P1 centers, i.e. H_{P1-P1} in Eq. 12. Thus, the same pulse sequence that enabled the time reversal of the P1 interaction, shown in Fig. S3, can be applied to the average NV interactions to transform \tilde{H} into $-\frac{1}{2}\tilde{H}$.

The complete sensing protocol utilizing NV ensembles is outlined as follows:

1. Optically polarize the NV centers into the $|0\rangle$ state.
2. Rotate the state via a $\pi/2$ pulse in the subspace $\{|0\rangle, |-1\rangle\}$.
3. Evolve under the average Hamiltonian \tilde{H} by alternating between the $\{|0\rangle, |-1\rangle\}$ subspace and $\{|-1\rangle, |1\rangle\}$ subspace.
4. Apply a small global rotation to the NV centers, $e^{i\epsilon S_x}$, where the angle ϵ is optimized as function of the evolution time.
5. Evolve backwards under $-\tilde{H}$ by (a) alternating between the two subspaces and (b) applying the pulse sequence shown in Fig. S3 within each subspace.
6. Apply the global sensing signal $e^{-i\phi S_z}$, where $S_z = \sum_i s_z^i$.
7. Evolve forward again under \tilde{H} , and measure the total polarization of the NV centers via optical excitation.

To our knowledge, implementing time reversal by applying pulse engineering sequences to *multiple subspaces* has not been previously proposed. Successfully demonstrating this technique, which we refer to as “subspace engineering”, and comparing it to more standard pulse sequences involving a single subspace, represents an exciting experimental prospect.

D. Atoms in an optical cavity

One of the most successful platforms for demonstrating entanglement-enhanced sensing consists of atoms coupled in an optical cavity [4, 5, 17]. Conventionally, this enhancement is achieved by evolving under collective large-spin interactions (e.g. the one-axis twisting Hamiltonian) to generate a squeezed state. However, this approach does not succeed for more general types of dynamics, arising in e.g. a multi-mode cavity [18] or via programmable interactions [19].

We consider the latter setting with a system of spin-1/2 atoms. The programmable spin-exchange interactions are described by an effective Hamiltonian [19]:

$$H = \sum_{i < j} J(r_{ij}) (\sigma_x^i \sigma_x^j + \sigma_y^i \sigma_y^j), \quad (22)$$

where the sign and magnitude $J(r_{ij})$ are controllable by laser drives. Motivated by Ref. [20], we select the interaction strength to be of the form

$$J(r_{ij}) = \begin{cases} (-1)^n |i - j|^s & \text{if } |i - j| = 2^n, n \in \mathbb{Z} \\ 0 & \text{otherwise} \end{cases} \quad (23)$$

where the parameter s interpolates between a quasi-one-dimensional geometry ($s < 0$) and a tree-like geometry ($s > 0$). Note that we include a mix of ferromagnetic and anti-ferromagnetic couplings. This is anticipation of initializing to protocol with a fully polarized initial state, $|\mathbf{0}\rangle = |+\rangle^{\otimes N}$; the anti-ferromagnetic interactions serve to raise the temperature this state.

Although local control is theoretically possible in this setup [21], it is most natural to realize our protocol with global controls. Numerical simulations for the sensitivity as a function of evolution time are depicted in Fig. S4. For $s < 0$, we observe that the sensitivity quickly reaches a saturation value that improves with system size $\sim N$, indicating a Heisenberg-like enhancement. Intriguingly, in the case of $s > 0$, we find a qualitatively different behavior: the sensitivity exhibits large fluctuations and does not improve systematically with system size. This suggests that the tree-like geometry does not lead to fully scrambling behavior. Understanding the subtle interplay between many-body dynamics and improved sensitivity for such non-trivial geometries would be an interesting future direction.

E. Superconducting qubits with analog interactions

Tremendous progress has been made in developing quantum processors based on 2D arrays of superconducting transmon qubits [22–24]. While such processors are often controlled with digital gates, we consider an implementation of our protocol which utilizes the intrinsic (analog) interactions between tunable-frequency qubits. In particular, when the qubits are brought on resonance, their interaction is described by a local XY model [24, 25],

$$H = J \sum_{\langle i, j \rangle} (\sigma_x^i \sigma_x^j + \sigma_y^i \sigma_y^j), \quad (24)$$

where the coupling strength $|J|$ is typically 10–100 MHz [26]. As demonstrated in Ref. [24], when the lattice of qubits is bipartite, the sign of interaction can be quite easily reversed by conjugating the evolution with π -pulses, i.e. $-H = (\prod_{i \in \mathcal{S}} \sigma_x^i) H (\prod_{i \in \mathcal{S}} \sigma_x^i)$, where \mathcal{S} is one part of the bipartite lattice. This reversibility, in addition to local rotations generated by microwave pulses, enables the realization of our protocol with local control.

In Fig. S4, we show numerical results for our protocol in a 2D array of up to 20 qubits. While the functional form of the early-time growth cannot be discerned, at larger sizes one expects the nearest-neighbor interactions to lead to ballistic growth of the form $\sim (Jt)^2$. Based on an estimate of this growth rate, a qubit lifetime of $T_1 \sim 20 \mu\text{s}$ [27], and a coupling strength $J \sim 50$ MHz [26], we predict that a fully scrambled state can be prepared with ~ 400 qubits, leading to a metrological gain of 20 dB. This would significantly surpass the current record for metrological gain of 11.8 dB, recently demonstrated via atoms in an optical cavity [5].

For comparison, a more conventional approach for obtaining a metrological gain in a digital quantum processor would be to prepare a GHZ state (the current record is a GHZ state with 60 qubits and a fidelity of 0.59) [3, 28]. It is natural to consider which of these strategies would lead to a larger metrological gain on realistic devices. On the one hand, the theoretical sensitivity for a GHZ state at equivalent sizes is a factor of two better than our protocol. Additionally, sensing based on a GHZ state requires two layers of entangling gates (i.e. the state preparation circuit and its inverse, assuming that robustness to noise is desired), whereas our protocol requires three steps of many-body evolution. On the other hand, our protocol is much more robust against control errors, since it does not require precisely calibrated two-qubit gates; indeed, such errors often represent a significant fraction of the total error [29]. Moreover, the total evolution time for implementing our protocol may be shorter, since the analog interactions are “always on”, thereby reducing the effect of decoherence [25]. Testing these advantages in practice would be of tremendous interest and may provide a useful tool for benchmarking large-scale quantum processors.

F. Trapped-ion quantum computer

Lastly, we consider an implementation of protocol on a trapped-ion quantum computer [30, 31]. Unlike the previous proposals which rely on analog evolution, we utilize discrete quantum gates to generate the many-body unitary U . Specifically, we construct circuits with interspersed layers of two-qubit and single-qubit gates. For the two-qubit gates, we choose $N/2$ pairs of qubits at random and apply the native Molmer-Sorensen interaction, $e^{i\frac{\pi}{4}\sigma_i^x\sigma_j^x}$, to each pair. This arrangement takes advantage of the all-to-all connectivity of trapped ions. For the single-qubit gates, we apply $e^{i\alpha_i\sigma_z^i}e^{i\frac{\pi}{4}\sigma_y^i}e^{i\beta_i\sigma_z^i}$, where $\alpha_i, \beta_i \in [0, 2\pi]$ are chosen from a uniform distribution. In Fig. S4(d), we plot numerical results for the sensitivity as function of circuit depth using the sensing protocol with local controls. Much like our previous results with analog evolution, we observe an initial rise in sensitivity, followed by saturation at $\eta \approx 2/N$. Owing to the all-to-all connectivity, the circuit depth to reach saturation scales favorably with system size; indeed, one expects it to occur in $\sim \log N$ layers at large system sizes.

As discussed in the main text, an important feature of our protocol is its robustness against coherent errors, which are considered to be a dominant error source in trapped-ion systems. Physically, such errors arise from low-frequency fluctuations in the laser drive amplitudes, causing imperfections in the rotation angles, i.e. $\theta_{ij} \rightarrow \theta'_{ij}$. These errors will limit the ability to prepare finely-tuned metrological states, including a GHZ state. However, in our protocol, if these errors can be time reversed they have essentially no impact on the achievable sensitivity—they would simply adjust the many-body unitary, $U \rightarrow U'$, and, at late times, this would still result in a fully scrambled state. Thus, at large system sizes and / or high coherent error rates, we expect our protocol to provide a larger metrological gain compared to sensing based on a GHZ state.

IV. DETAILS ON STOCHASTIC MODEL USED FOR LARGE-SCALE NUMERICAL STUDIES

In this section, we introduce a stochastic model for operator growth dynamics which allows us to predict the large-scale behavior of our protocol for the two proposed systems of spin defects. The model is inspired by previous work on quantum information scrambling, where it has been argued that growth of operators under *long-range* Hamiltonian dynamics can be qualitatively captured at long timescales by stochastic transitions [32–34]. For our purposes, we model these transitions using Haar-random gates and determine the probability of each gate based on the strength of the spin interactions.

In more detail, consider a Hamiltonian composed of two-body interactions, $H = \sum_{ij\mu} h_{ij}^\mu$, where h_{ij}^μ indicates a particular two-body operator acting on qubits i and j . Our model consists of mapping the analog evolution $U = e^{-iHt}$ to a circuit composed of D time steps, $\tilde{U} = U_D \cdots U_2 U_1$. In each time step, we apply a set of two-qubit, Haar-random gates, where the probability of a gate occurring between qubits i and j is $P_{ij} = \delta t \sum_\mu |h_{ij}^\mu|^2$. We set $\delta t \ll 1/J_{\text{typ}}$, where J_{typ} is the typical interaction strength, such that there is a low density of gates per time step.

A key feature of Haar-random gates is that, for measuring certain quantities, the average over Haar-random gates is equivalent to the average over random Clifford gates [35]. The average sensitivity of our protocol (with either global or local control) represents such a quantity; this results from the fact that the

sensitivity contains three copies of U and U^\dagger , and Clifford unitaries form a 3-design for qubits [36–38]. Thus, the average sensitivity of the stochastic model can be computed efficiently using Clifford numerics.

We apply the stochastic model to predict the sensitivity of our protocol for either local or global control. For the local protocol, we compute the sensitivity $\eta_{\phi=0}$ by measuring the average polarization density $P(S_z)$ of $\tilde{U}^\dagger V \tilde{U} |\mathbf{0}\rangle$ [see Eq. (5)]. This is easily accomplished by evolving V in the Heisenberg picture with Clifford gates, and then counting the number of σ_x and σ_y operators within the Pauli string $V(t)$.

Computing the sensitivity for the global protocol is somewhat more involved. We begin by expressing the mean outcome as

$$\langle S_x \rangle_\phi = \langle \mathbf{0} | U^\dagger e^{i\epsilon S_x} U e^{i\phi S_z} U^\dagger S_x U e^{-i\phi S_z} U^\dagger e^{-i\epsilon S_x} U | \mathbf{0} \rangle, \quad (25)$$

where $\vec{S} = \frac{1}{2} \sum_i \vec{\sigma}^i$ are global spin-1/2 operators. To proceed, we expand the operator S_x in a Pauli basis:

$$\langle S_x \rangle_\phi = \frac{1}{2} \sum_{a,b \in \{0,1\}^N} \sum_{i=1}^N c_a c_b^* \langle \mathbf{0} | U^\dagger P_a U e^{i\phi S_z} U^\dagger \sigma_x^i U e^{-i\phi S_z} U^\dagger P_b U | \mathbf{0} \rangle, \quad (26)$$

where $P_a = \prod_{i \in a} \sigma_x^i$ contains σ_x^i on all sites for which a is non-zero, $c_a = (i \sin(\epsilon/2))^{|a|} (\cos(\epsilon/2))^{N-|a|}$, and $|a| = \sum_i a_i$ is the Hamming weight of a . For a Clifford unitary U , the state $U^\dagger P_b U |\mathbf{0}\rangle$ is an eigenstate of S_z . This allows us to pull the factors of $e^{\pm i\phi S_z}$ outside the expectation value, giving

$$\langle S_x \rangle_\phi = \frac{1}{2} \sum_{a,b \in \{0,1\}^N} \sum_{i=1}^N c_a c_b^* e^{i\phi_{ab}} \langle \mathbf{0} | U^\dagger P_a \sigma_x^i P_b U | \mathbf{0} \rangle, \quad (27)$$

where $\phi_{ab} = \phi(S_z\{U^\dagger P_a U\} - S_z\{U^\dagger P_b U\})$ and $S_z\{P\} = \#$ of σ_x, σ_y in P . With high probability, the matrix element $\langle \mathbf{0} | U^\dagger P_a \sigma_x^i P_b U | \mathbf{0} \rangle$ is non-zero if and only if $P_a \sigma_x^i P_b = \mathbf{1}$. With this simplification, we have

$$\langle S_x \rangle_\phi \approx \frac{1}{2} \sum_{a \in \{0,1\}^N} \sum_{i=1}^N |c_a|^2 (i \tan(\epsilon/2))^{|b_i|-|a|} e^{i\phi_{ab_i}}, \quad (28)$$

where b_i differs from a only on the i^{th} bit. We note that $|c_a|^2$ is the probability of sampling $|a|$ from a binomial process with N draws of probability $\sin^2(\epsilon/2)$, and thus we can approximate the above expression using Monte Carlo sampling.

In summary, the full procedure for estimating $\langle S_x \rangle_\phi$ is as follows:

1. Sample a from a binomial distribution and i from a uniform distribution. The bitstring b_i is immediately given by flipping a on the i^{th} bit.
2. Compute $\phi_{ab} = \phi(S_z\{U^\dagger P_a U\} - S_z\{U^\dagger P_b U\})$ by time evolving X_a and X_b under a Clifford circuit.
3. Average the quantity $(i \tan \epsilon)^{|b_i|-|a|} e^{i\phi_{ab_i}}$ over many samples.

We estimate the sensitivity via $\eta_{\phi=0}^{-1} \equiv (\partial_\phi \langle S_x \rangle_\phi / \Delta S_{x,\phi})_{\phi=0} \approx \langle S_x \rangle_\phi / \sqrt{N}$, where $\phi \ll 1$, and for circuits with Haar-random gates, on average, $\langle S_x \rangle_{\phi=0}$ and $(\Delta S_x)_{\phi=0} = \sqrt{N}/2$.

To benchmark the stochastic model, we calculate the sensitivities for up to $N = 20$ spins for (i) the local protocol based the interactions of the hybrid spin system, and (ii) the global protocol based on the interactions of an ensemble of NV centers. In Fig. S5, we compare these results to the the sensitivities obtained from simulations with exact dynamics. The two methods yield good qualitative agreement for both the local and global protocols. Moreover, by matching the growth rate at early times, we can estimate the conversion factor between discrete time steps in the stochastic model and evolution time for the exact dynamics. Utilizing this conversion factor, we simulate the behavior of much larger spin systems, as shown in the insets of Fig. 4 of the main text. We expect the results of the stochastic model to provide a good approximation for the exact behavior of the experimental system, in a regime that would be intractable to simulate with the exact dynamics.

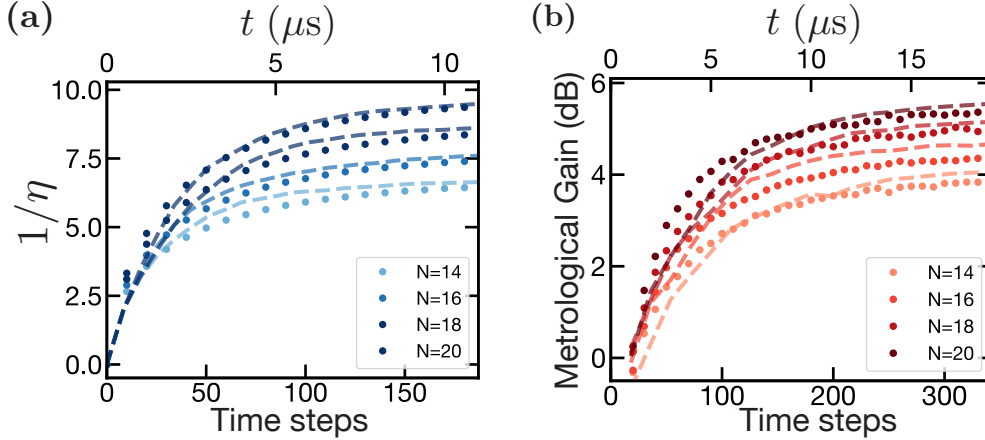


FIG. S5. Comparison between the stochastic model (solid lines) and exact dynamics (dashed) for the two proposed spin models at small sizes. (a) The sensitivity of the local protocol applied to the hybrid spin system with single NV center surrounded by a cluster of P1 centers. The density of spin defects is 100 ppm dynamics, and their interactions are governed by \hat{H}^+ in Eq. 14. (b) The metrological gain of the global protocol applied to an ensemble of NV centers. The density of the NV centers is 100 ppm, and their dynamics are governed by \hat{H} in Eq. 20. The results for the stochastic model are plotted as a function of the number of discrete time steps, and the results for the exact dynamics are plotted with respect to continuous time evolution. By comparing the results, we estimate the conversion factor between discrete steps and continuous evolution time. The results for the stochastic model are averaged over $\sim 10^4$ realizations (including different positional configurations and Clifford circuits), and the results for the exact dynamics are averaged over ~ 10 positional configurations.

V. DETAILED ANALYSIS OF THE EFFECTS OF NOISE AND DECOHERENCE

We now provide a detailed accounting of the effect of experimental errors on our sensing protocols. We begin with a brief discussion of readout and initialization errors, which as mentioned in the main text, decrease the sensitivity by only a constant factor. We then turn to incoherent errors during time evolution, and, borrowing from the results of Ref. [39], derive the suppression factor indicated in the main text.

Readout errors have a particularly small effect on our protocol. For the local control protocol, a local readout error rate γ_r suppresses the expectation value of V by a constant factor, $\langle V \rangle_\phi \rightarrow (1 - \gamma_r) \langle V \rangle_\phi$. A similar suppression occurs for the global protocol, $\langle S_x \rangle_\phi \rightarrow (1 - \gamma_r) \langle S_x \rangle_\phi$, since S_x is a sum of single-body operators. In both cases, the sensitivity is suppressed by the same factor, $\eta_\phi^{-1} \rightarrow (1 - \gamma_r) \eta_\phi^{-1}$.

To address initialization errors, consider performing the protocol with an initial density matrix ρ instead of $|0\rangle\langle 0|$. We denote the mean polarization of ρ as $\text{tr}(\rho S_z) = (1 - \gamma_i)N/2$, where γ_i quantifies the local initialization error rate. We also suppose that the polarization distribution of ρ has width $\lesssim \sqrt{N}$, which is appropriate for local initialization errors. After butterfly state preparation, the density matrix becomes

$$\left(\frac{\mathbb{1} + iV(t)}{\sqrt{2}} \right) \rho \left(\frac{\mathbb{1} - iV(t)}{\sqrt{2}} \right) = \frac{1}{2} (\rho + V(t)\rho V(t) + i[V(t)\rho - \rho V(t)]), \quad (29)$$

where $V(t) = U^\dagger V U$. The first and second terms correspond to the two trajectories of the butterfly state, and the third term to the coherence between them. As in the error-free case, for small angles $\phi \lesssim 1/\sqrt{N}$ the rotation $e^{-i\phi S_z}$ simply applies an overall phase to each trajectory of the butterfly state. Working in the late time regime where $e^{i\phi S_z} V(t) \rho \approx V(t) \rho$, this leads to the density matrix

$$e^{i\phi S_z} \left(\frac{\mathbb{1} + iV(t)}{\sqrt{2}} \right) \rho \left(\frac{\mathbb{1} - iV(t)}{\sqrt{2}} \right) e^{-i\phi S_z} \approx \frac{1}{2} \left(\rho + V(t)\rho V(t) + i \left[e^{-i\phi(1-\gamma_i)N/2} V(t)\rho - e^{i\phi(1-\gamma_i)N/2} \rho V(t) \right] \right). \quad (30)$$

As in the error-free case, only the third term (in square brackets) will contribute to the final expectation value of V . Applying the final unitary and taking the expectation value gives

$$\langle V \rangle_\phi \approx \sin \left(\phi \frac{(1 - \gamma_i)N}{2} \right). \quad (31)$$

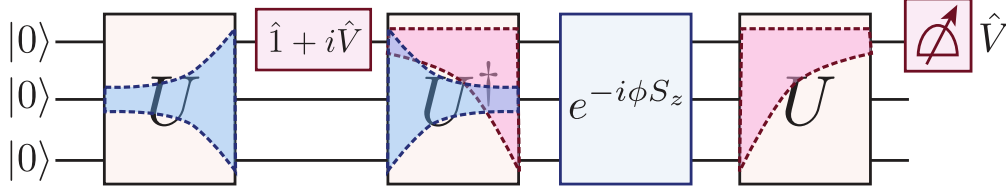


FIG. S6. Illustration of the effect of errors on our sensing protocol. Errors within the light-cone of V (red dashed areas) suppress the coherence between the two trajectories of the butterfly state. Errors within the light-cone of a local polarization operator σ_i^z (blue dashed areas, shown for a representative polarization operator) suppress the polarization of the first trajectory of the butterfly state. The sensitivity of the protocol is affected by both types of errors, and is thus suppressed proportional to the local error rate γ multiplied by the space-time volume of the four light-cones. Note that initialization and readout errors can be included in this diagram as well; since they only act at times when the light-cones have size one, they have only an $\mathcal{O}(1)$ effect on the sensitivity.

Taking the derivative with respect to ϕ , we see that the sensitivity is decreased by only a constant factor relative to the error-free case, $\eta_\phi^{-1} \rightarrow (1 - \gamma_i)\eta_\phi^{-1}$.

We now turn to incoherent errors during time evolution. As mentioned in the main text, incoherent errors have two effects on the protocol: they suppress the mean polarization in the first trajectory of the butterfly state, and they suppress the coherence between the two butterfly trajectories. Both effects suppress the sensitivity, the first by suppressing the first derivative of $\langle V \rangle_\phi$ with respect to ϕ (similar to initialization errors), and the second by suppressing the overall magnitude of $\langle V \rangle_\phi$ (similar to readout errors). However, unlike initialization and readout errors, errors during time evolution occur when the state is highly-entangled and thus have a stronger effect (Fig. S6).

To explore this in more detail, let us replace the unitary evolution $\rho \rightarrow U\rho U^\dagger$ by evolution under a noisy quantum channel, $\rho \rightarrow \mathcal{E}_\gamma\{\rho\}$. For analog evolution, the quantum channel might be generated by a Lindbladian, $\mathcal{E}_\gamma = e^{\mathcal{L}_\gamma t}$, where \mathcal{L}_γ includes both Hamiltonian evolution and local noise operators with strength γ . For digital evolution, the quantum channel might correspond to a sequence of unitary gates interspersed with local noise channels of strength γ . In any case, we will assume that the quantum channel corresponding to U^\dagger is the *conjugate* of the channel corresponding to U , defined via $\text{tr}(M \cdot \mathcal{E}_\gamma\{\rho\}) = \text{tr}(\mathcal{E}_\gamma^\dagger\{M\} \cdot \rho)^c$. This reduces to standard time reversal when the evolution is unitary.

Let us now analyze the sensitivity of the protocol at $\phi = 0$. We have

$$\partial_\phi \langle V \rangle_\phi = \text{Im} \left[\text{tr} \left(S_z \cdot \mathcal{E}_\gamma^\dagger\{V\} \cdot \mathcal{E}_\gamma^\dagger \left\{ \frac{\mathbb{1} + iV}{\sqrt{2}} \mathcal{E}_\gamma\{|\mathbf{0}\rangle\langle\mathbf{0}|\} \frac{\mathbb{1} - iV}{\sqrt{2}} \right\} \right) \right], \quad (32)$$

where we apply (the conjugate of) the final time evolution to the measurement operator V instead of the quantum state. As in the error-free case, we can drop terms that contain an odd number of V . Moreover, terms where a single V operator appears in between S_z and the initial state $|\mathbf{0}\rangle\langle\mathbf{0}|$ can also be dropped if the system is fully scrambled after application of \mathcal{E}_γ . These correspond to the polarization of the second trajectory of the butterfly state or, in other language, to OTOCs that have decayed to zero. Dropping these terms gives

$$\partial_\phi \langle V \rangle_\phi \approx \text{tr}(S_z \cdot \mathcal{E}_\gamma^\dagger\{V\} \cdot \mathcal{E}_\gamma^\dagger\{V \cdot \mathcal{E}_\gamma\{|\mathbf{0}\rangle\langle\mathbf{0}|\}\}). \quad (33)$$

Now, note that the initial state $|\mathbf{0}\rangle\langle\mathbf{0}|$ can be decomposed as a sum of stabilizers as

$$|\mathbf{0}\rangle\langle\mathbf{0}| = \frac{1}{2^N} \sum_{s \in \{0,1\}^N} \bigotimes_{i=1}^N (\sigma_i^z)^{s_i}. \quad (34)$$

To good approximation, only the single-body stabilizers σ_i^z contribute to the expectation value, since they can “contract” with the same stabilizer in S_z . Keeping only these stabilizers, we have

$$\partial_\phi \langle V \rangle_\phi \approx \frac{1}{2} \sum_{i=1}^N \frac{1}{2^N} \text{tr}(\sigma_i^z \cdot \mathcal{E}_\gamma^\dagger\{V\} \cdot \mathcal{E}_\gamma^\dagger\{V \cdot \mathcal{E}_\gamma\{\sigma_i^z\}\}), \quad (35)$$

^c On a technical level, this requires assuming that the noise is unital. We expect non-unitality of the noise channel to contribute at sub-leading order in γ ; see the supplemental material of Ref. [39] for a full discussion.

which is our final approximation. The approximation resembles a “doubled” version of the Loschmidt echo, which depends on both the fidelities of a local operator σ_i^z at time zero and a local operator V at time t .

To understand how this approximation depends on the local noise rate γ , we invoke the results of Ref. [39]. There, it was argued that for ergodic many-body quantum dynamics, the decay of the Loschmidt echo,

$$\mathcal{N}_\gamma(M) = \frac{1}{2^N} \text{tr}(M \cdot \mathcal{E}_\gamma^\dagger \{ \mathcal{E}_\gamma \{ M \} \}), \quad (36)$$

is controlled by the effective space-time volume of the time-evolved operator M ,

$$\mathcal{N}_\gamma(M) \approx \exp(-2\gamma \text{Vol}[M(0 \rightarrow t)]). \quad (37)$$

Here, the space-time volume is defined as the integral over time of the *size* of the operator M ,

$$\text{Vol}[M(0 \rightarrow t)] = \int_0^t dt' \mathcal{S}(t'), \quad (38)$$

where the size is given by the (average) number of qubits that M acts upon,

$$\mathcal{S}(t') = \sum_P |c_P(t')|^2 \mathcal{S}_P, \quad (39)$$

where $M(t') = \sum_P c_P(t') \sigma_P$ is the Pauli decomposition of M at time t' and $\mathcal{S}_P = (\# \text{ of } \sigma_x, \sigma_y, \sigma_z \text{ in } P)$ is the weight of the Pauli operator P . In principle, one should compute this volume for time evolution under the noisy quantum channel [39]. However, to estimate the leading order dependence in γ we can substitute the volume under unitary evolution. In short-range interacting systems, the space-time volume is proportional to the volume of the operators’ light-cone, and Eq. (37) simply states that only errors within the light-cone contribute to the decay of the Loschmidt echo.

We can straightforwardly apply this approximation to the sensitivity in Eq. (40). The first quantum channel (applied to σ_i^z) contributes a factor $\gamma \text{Vol}[\sigma_i^z(0 \rightarrow t)]$ to the exponent. The final quantum channel (applied to V) contributes a factor $\gamma \text{Vol}[V(0 \rightarrow t)]$. The only subtlety is the middle quantum channel (applied to $V \cdot \mathcal{E}_\gamma \{ \sigma_i^z \}$). This contributes a factor proportional to the space-time volume of the *product* of σ_i^z and V , where the former is local at the end of the evolution and the latter at the beginning. In a slight abuse of notation, we denote this quantity as $\text{Vol}[\sigma_i^z(t \rightarrow 0) \cup V(0 \rightarrow t)]$. Putting it all together, we estimate

$$\partial_\phi \langle V \rangle_\phi \approx \frac{1}{2} \sum_{i=1}^N \exp(-\gamma (\text{Vol}[\sigma_i^z(0 \rightarrow t)] + \text{Vol}[V(0 \rightarrow t)] + \text{Vol}[\sigma_i^z(t \rightarrow 0) \cup V(0 \rightarrow t)])). \quad (40)$$

The relevant light-cones are depicted visually in Fig. S6. Note that the volume of the product will (typically) be upper bounded by the sum of the individual volumes. This gives a lower bound on the sensitivity,

$$\begin{aligned} \partial_\phi \langle V \rangle_\phi &\gtrsim \left(\frac{1}{2} \sum_{i=1}^N \exp(-2\gamma \text{Vol}[\sigma_i^z(0 \rightarrow t)]) \right) \cdot \exp(-2\gamma \text{Vol}[V(0 \rightarrow t)]) \\ &= \frac{N}{2} \cdot \overline{\mathcal{N}_\gamma(\sigma_i^z)} \cdot \mathcal{N}_\gamma(V) \end{aligned} \quad (41)$$

The first term is given by $N/2$ multiplied by the average Loschmidt echo of σ_i^z . This corresponds to the loss in polarization of the first butterfly trajectory. The second term is given by the Loschmidt echo of V , and corresponds to the loss of coherence between the first and second trajectories of the butterfly state.

Let us consider this final expression for a system with local interactions in d dimensions. We assume local operators spread ballistically with a butterfly velocity v_B , resulting in an operator size $S(t) \approx (v_B t)^d$ and a volume $\text{Vol}[V(0 \rightarrow t)] \approx \text{Vol}[\sigma_i^z(0 \rightarrow t)] \approx \frac{1}{(d+1)v_B} (v_B t)^{d+1}$. To reach a fully scrambled state, we take $t \approx N^{1/d}/v_B$. This leads to an overall sensitivity,

$$\partial_\phi \langle V \rangle_\phi \gtrsim \frac{N}{2} \exp\left(-\frac{4}{d+1} \frac{\gamma}{v_B} N^{\frac{d+1}{d}}\right). \quad (42)$$

We utilize this expression to estimate the sensitivity under decoherence for the dipolar Rydberg atoms and superconducting qubits.

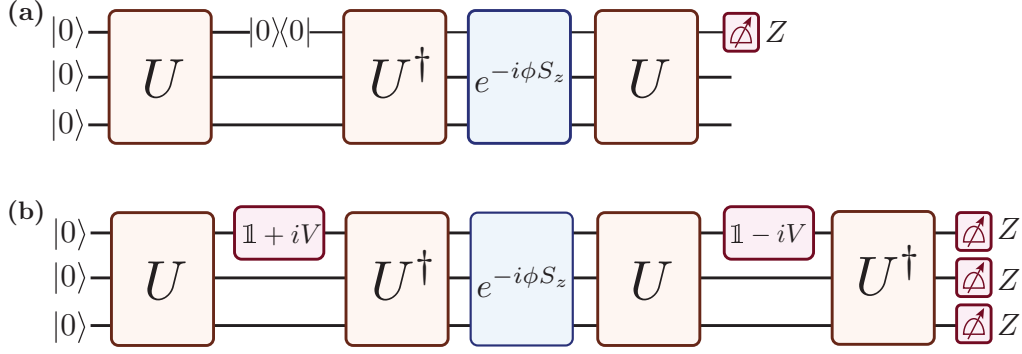


FIG. S7. Two protocols for measuring the *real* part of $\Phi(\phi)$. (a) The first protocol is identical to the original protocol with local controls [Fig. 1(a) of the main text], except we replace the local rotation, $e^{i\frac{N}{2}4V} \sim \mathbb{1} + iV$, with a local projection, $|0\rangle\langle 0| \sim \mathbb{1} + Z$. (b) The second protocol, which we dub a “double echo”, involves applying the butterfly state preparation circuit and its inverse. The final state is measured in the computational basis, and either the return probability to the initial state or the average polarization is computed. This approach may be applied with either local or global controls to prepare the butterfly state.

VI. EXPERIMENTAL PROTOCOL TO MEASURE THE OPPOSITE QUADRATURE

As discussed in the previous section, the protocols shown in the main text (i.e. Fig. 1 and 3) are directly related to the imaginary part of the characteristic function $\Phi(\phi)$ of the polarization distribution $P(S_z)$. This implies that they achieve a high sensitivity only at certain values of ϕ , including, most notably, $\phi = 0$. In order to maintain a high sensitivity over a continuous range of ϕ , it is necessary to measure the opposite quadrature—i.e. the real part of the characteristic function.

There are two straightforward modifications of our protocol that achieve this goal, depicted in Fig. S7. The first approach, which applies only to the protocol with local controls, is to replace the local rotation by a *projection*, e.g. $(\mathbb{1} + V)/2$ for a Pauli operator V . The measurement outcome then becomes

$$\begin{aligned} \langle V \rangle_\phi &= \frac{1}{2} \langle \mathbf{0} | V(t) | \mathbf{0} \rangle - \frac{1}{2} \langle \mathbf{0} | V(t) e^{i\phi S_z} V(t) e^{-i\phi S_z} V(t) | \mathbf{0} \rangle \\ &\quad + \text{Re} \left[e^{i\phi \frac{N}{2}} \langle \mathbf{0} | V(t) e^{-i\phi S_z} V(t) | \mathbf{0} \rangle \right] \\ &= \text{Re} \left[e^{i\phi \frac{N}{2}} \Phi(\phi) \right], \end{aligned} \quad (43)$$

where $\Phi(\phi)$ is defined below Eq. (3), and, in the second line, we assume that the first two terms have vanishing expectation values^d. While conceptually simple, measuring the real part of $\Phi(\phi)$ in this way requires the ability to reset an individual qubit during the execution of the protocol. Alternatively, one can delay the projection to the end of the protocol by swapping in an ancilla qubit in the state $|0\rangle$ (taking $V = \sigma^z$), and post-selecting on the final state of the ancilla qubit.

Our second approach, analogous to a standard Loschmidt echo, is to perform the full inverse of the state preparation procedure, as shown in Fig. S7. This approach can be applied with either local or global controls, but, for specificity, let us focus on the variant with local controls. The conceptually simplest quantity to analyze is the return probability, P_0 , given by

$$\begin{aligned} P_0 &= \frac{1}{4} \left| \langle \mathbf{0} | (\mathbb{1} - iV(t)) e^{-i\phi S_z} (\mathbb{1} + iV(t)) | \mathbf{0} \rangle \right|^2 \\ &= \frac{1}{4} \left| e^{-i\phi \frac{N}{2}} + \langle \mathbf{0} | V(t) e^{i\phi S_z} V(t) | \mathbf{0} \rangle \right|^2 \\ &= \frac{1}{4} \left(1 + |\Phi(\phi)|^2 + 2\text{Re} \left[e^{-i\phi \frac{N}{2}} \Phi(\phi) \right] \right) \end{aligned} \quad (44)$$

^d The first two terms may also be directly cancelled by projecting onto the opposite state, i.e. using $(\mathbb{1} - V)/2$, and measuring $-V$. Averaging this outcome with Eq. (44) leaves only the final term, $\text{Re} [e^{i\phi N} \Phi(\phi)]$.

The real part of $\Phi(\phi)$ can easily be inferred by combining this quantity with the outcome from Eq. (3). This approach directly generalizes to the case of global controls by replacing the local rotation with a global one, e.g. $e^{i\epsilon S_x}$. In either case, an additional many-body unitary (i.e. 2 copies of U and U^\dagger) is required compared to the previous protocols.

We note that, although measuring the return probability is straightforward to analyze, it is highly sensitive to readout errors. In practice, therefore, it is better to measure either the average polarization or polarization distribution of the final state, both of which display qualitatively similar behavior to the return probability. In particular, if the external signal applies a relative phase between the two components of the butterfly state, $|\mathbf{0}\rangle$ and $V(t)|\mathbf{0}\rangle$, then the polarization distribution of the final state features two peaks—a fully polarized state and a random state centered about zero polarization—with a relative height that oscillates as function of ϕ . Readout noise broadens the two peaks, but they remain extensively separated.

-
- [1] E. Davis, G. Bentsen, and M. Schleier-Smith, *Physical review letters* **116**, 053601 (2016).
 - [2] T. Macrì, A. Smerzi, and L. Pezzè, *Physical Review A* **94**, 010102 (2016).
 - [3] G. J. Mooney, G. A. White, C. D. Hill, and L. C. Hollenberg, *Journal of Physics Communications* **5**, 095004 (2021).
 - [4] Z. Li, S. Colombo, C. Shu, G. Velez, S. Pilatowsky-Cameo, R. Schmied, S. Choi, M. Lukin, E. Pedrozo-Peñañiel, and V. Vuletić, *Science* **380**, 1381 (2023).
 - [5] S. Colombo, E. Pedrozo-Peñañiel, A. F. Adiyatullin, Z. Li, E. Mendez, C. Shu, and V. Vuletić, *Nature Physics* **18**, 925 (2022).
 - [6] G. Goldstein, P. Cappellaro, J. R. Maze, J. Hodges, L. Jiang, A. S. Sørensen, and M. Lukin, *Physical review letters* **106**, 140502 (2011).
 - [7] M. Block, B. Ye, B. Roberts, S. Chern, W. Wu, Z. Wang, L. Pollet, E. J. Davis, B. I. Halperin, and N. Y. Yao, *arXiv preprint arXiv:2301.09636* (2023).
 - [8] V. Khemani, A. Vishwanath, and D. A. Huse, *Physical Review X* **8**, 031057 (2018).
 - [9] C. Chen, G. Bornet, M. Bintz, G. Emperauger, L. Leclerc, V. S. Liu, P. Scholl, D. Barredo, J. Hauschild, S. Chatterjee, *et al.*, *Nature* **616**, 691 (2023).
 - [10] G. Bornet, G. Emperauger, C. Chen, B. Ye, M. Block, M. Bintz, J. A. Boyd, D. Barredo, T. Comparin, F. Mezzacapo, *et al.*, *arXiv preprint arXiv:2303.08053* (2023).
 - [11] A. V. Gorshkov, S. R. Manmana, G. Chen, E. Demler, M. D. Lukin, and A. M. Rey, *Physical Review A—Atomic, Molecular, and Optical Physics* **84**, 033619 (2011).
 - [12] S. De Léséleuc, D. Barredo, V. Lienhard, A. Browaeys, and T. Lahaye, *Physical Review A* **97**, 053803 (2018).
 - [13] C. Zu, F. Machado, B. Ye, S. Choi, B. Kobrin, T. Mittiga, S. Hsieh, P. Bhattacharyya, M. Markham, D. Twitchen, *et al.*, *Nature* **597**, 45 (2021).
 - [14] A. Jarmola, V. Acosta, K. Jensen, S. Chemerisov, and D. Budker, *Physical review letters* **108**, 197601 (2012).
 - [15] J. Choi, H. Zhou, H. S. Knowles, R. Landig, S. Choi, and M. D. Lukin, *Physical Review X* **10**, 031002 (2020).
 - [16] G. Kucsko, S. Choi, J. Choi, P. C. Maurer, H. Zhou, R. Landig, H. Sumiya, S. Onoda, J. Isoya, F. Jelezko, *et al.*, *Physical review letters* **121**, 023601 (2018).
 - [17] E. Pedrozo-Peñañiel, S. Colombo, C. Shu, A. F. Adiyatullin, Z. Li, E. Mendez, B. Braverman, A. Kawasaki, D. Akamatsu, Y. Xiao, *et al.*, *Nature* **588**, 414 (2020).
 - [18] V. D. Vaidya, Y. Guo, R. M. Kroeze, K. E. Ballantine, A. J. Kollár, J. Keeling, and B. L. Lev, *Physical Review X* **8**, 011002 (2018).
 - [19] A. Periwal, E. S. Cooper, P. Kunkel, J. F. Wienand, E. J. Davis, and M. Schleier-Smith, *Nature* **600**, 630 (2021).
 - [20] G. Bentsen, T. Hashizume, A. S. Buyskikh, E. J. Davis, A. J. Daley, S. S. Gubser, and M. Schleier-Smith, *Physical review letters* **123**, 130601 (2019).
 - [21] B. Swingle, G. Bentsen, M. Schleier-Smith, and P. Hayden, *Physical Review A* **94**, 040302 (2016).
 - [22] F. Arute, K. Arya, R. Babbush, D. Bacon, J. C. Bardin, R. Barends, R. Biswas, S. Boixo, F. G. Brandao, D. A. Buell, *et al.*, *Nature* **574**, 505 (2019).
 - [23] Y. Kim, A. Eddins, S. Anand, K. X. Wei, E. Van Den Berg, S. Rosenblatt, H. Nayfeh, Y. Wu, M. Zaletel, K. Temme, *et al.*, *Nature* **618**, 500 (2023).
 - [24] J. Braumüller, A. H. Karamlou, Y. Yanay, B. Kannan, D. Kim, M. Kjaergaard, A. Melville, B. M. Niedzielski, Y. Sung, A. Vepsäläinen, *et al.*, *Nature Physics* **18**, 172 (2022).
 - [25] T. I. Andersen, N. Astrakhantsev, A. Karamlou, J. Berndtsson, J. Motruk, A. Szasz, J. A. Gross, T. Westerhout, Y. Zhang, E. Forati, *et al.*, *arXiv preprint arXiv:2405.17385* (2024).
 - [26] B. Foxen, C. Neill, A. Dunsworth, P. Roushan, B. Chiaro, A. Megrant, J. Kelly, Z. Chen, K. Satzinger, R. Barends, *et al.*, *Physical Review Letters* **125**, 120504 (2020).
 - [27] E. Rosenberg, T. Andersen, R. Samajdar, A. Petukhov, J. Hoke, D. Abanin, A. Bengtsson, I. Drozdov, C. Er-

- ickson, P. Klimov, *et al.*, arXiv preprint arXiv:2306.09333 (2023).
- [28] Z. Bao, S. Xu, Z. Song, K. Wang, L. Xiang, Z. Zhu, J. Chen, F. Jin, X. Zhu, Y. Gao, *et al.*, arXiv preprint arXiv:2401.08284 (2024).
 - [29] X. Mi, P. Roushan, C. Quintana, S. Mandra, J. Marshall, C. Neill, F. Arute, K. Arya, J. Atalaya, R. Babbush, *et al.*, *Science* **374**, 1479 (2021).
 - [30] I. Pogorelov, T. Feldker, C. D. Marciniak, L. Postler, G. Jacob, O. Kriegelsteiner, V. Podlesnic, M. Meth, V. Negnevitsky, M. Stadler, *et al.*, *PRX Quantum* **2**, 020343 (2021).
 - [31] L. Egan, D. M. Debroy, C. Noel, A. Risinger, D. Zhu, D. Biswas, M. Newman, M. Li, K. R. Brown, M. Cetina, *et al.*, *Nature* **598**, 281 (2021).
 - [32] X. Chen and T. Zhou, *Physical Review B* **100**, 064305 (2019).
 - [33] T. Zhou, S. Xu, X. Chen, A. Guo, and B. Swingle, *Physical review letters* **124**, 180601 (2020).
 - [34] T. Zhou and B. Swingle, *Nature communications* **14**, 3411 (2023).
 - [35] A. Nahum, S. Vijay, and J. Haah, *Physical Review X* **8**, 021014 (2018).
 - [36] Z. Webb, arXiv preprint arXiv:1510.02769 (2015).
 - [37] R. Kueng and D. Gross, arXiv preprint arXiv:1510.02767 (2015).
 - [38] H. Zhu, *Physical Review A* **96**, 062336 (2017).
 - [39] T. Schuster and N. Y. Yao, *Physical Review Letters* **131**, 160402 (2023).